

Asymmetric polaron picture for the quantum Rabi model

Feng Qiao,^{1,2} Qiu-Yi Chen,^{1,2} and Zu-Jian Ying^{1,2,*}

¹*School of Physical Science and Technology, Lanzhou University, Lanzhou 730000, China*

²*Key Laboratory for Quantum Theory and Applications of MoE,*

Lanzhou Center for Theoretical Physics, Lanzhou University, Lanzhou 730000, China

The experimental access to ultra-strong couplings in light-matter interactions has made the quantum phase transition (QPT) in the quantum Rabi model practically relevant, while the physics of the QPT has not yet been fully explored. The polaron picture is a method capable of analyzing in the entire coupling regime and extracting the essential physics behind the QPT. However, the asymmetric deformation of polarons is missing in the current polaron picture. In the present work we propose an improved variational method in asymmetric polaron picture (APP). Our APP not only increases the method accuracy but also reveals more underlying physics concerning the QPT. We find that in the ground state both the polarons and antipolarons are asymmetrically deformed to a large extent, which leads to a richer phase diagram. We also analyze the first excited state in which we unveil an asymmetry direction reversal for the polarons and an attraction/replusion transition differently from the ground state. Finally, we apply the APP in quantum Fisher information analysis and critical coupling extraction, the improvements indicate that the polaron asymmetry makes a considerable contribution to the quantum resource in quantum metrology and plays an unneigligible role in the QPT. Our results and mechanism clarifications expose more subtle energy competitions and abundant physics, and the method potentially might have broader applications in light-matter interactions.

PACS numbers:

I. INTRODUCTION

The past two decades have seen the fast growing of the field of light-matter interaction in the frontiers of modern quantum physics. Both the theoretical progresses [1–4] and experimental advances [5–21] have brought much attention to the quantum Rabi model (QRM) [22–24] which is a most fundamental model of light-matter interactions. Indeed, the milestone work [1] revealing the integrability of the QRM has induced a massive dialogue [2] between mathematics and physics [1–4, 25–117]. On the other hand, the experimental access to ultra-strong [5–19, 21, 106] and deep-strong [17, 19, 49, 118] couplings has found the indispensable role of the counter-rotating terms [82] which renders the QRM to be more important. The QRM is particularly interesting also due to the fact that it possesses a finite-component quantum phase transition (QPT) [4, 25–53] as in many-body systems [29, 34]. Such a finite-component QPT can be practically applied in critical quantum metrology [30–33, 43, 54–68].

In the afore-mentioned dialogue between mathematics and physics [2], various approaches and methods [3] have been developed for investigations on the QRM and its extensions, such as exact solution in Bargmann-space representation [1], Bogoliubov transformation [72], exact diagonalization [36, 40], the rotating-wave approximation (RWA) [119], the generalized RWA [120], symmetry analysis [30, 37, 41, 43, 73, 101–103], the adiabatic approximation [121], the generalized variational method [98, 99], Schrieffer-Wolff transforma-

tion [27, 34], the mean-photon-number-dependent variational method [97], mean-field method [28, 50], variational displaced coherent state method [69, 80, 92, 122], the polaron picture [26, 36, 38, 71], and so on. These methods have made undeniable contributions in the road to the numerous findings including integrability [1], hidden symmetry [73, 101–103], various patterns of symmetry breaking [35–37], finite-component QPTs [4, 25–53], multicriticalities and multiple points [36–39], universality classification [27, 29, 34, 37, 39, 43], spectral collapse [71, 77, 85–87] and stabilization [32], photon blockade effect [88, 89], spectral conical intersections [90], classical-quantum correspondence [81], single-qubit conventional and unconventional topological phase transitions [37–41], coexistence and simultaneous occurrence of Landau-class and topological-class phase transitions [37, 39, 41, 43], robust topological feature against nonhermiticity [42, 43], squeezing and critical resources for quantum metrology [30–33, 43, 54–68], and so forth.

Essentially, many of these achievements are in a direct or indirect connection with the QPT originally found in the QRM [4, 25–53]. An effective method in the investigation of the QPT in the QRM is the variational method of polaron picture, which is valid with both high accuracy and clear physical picture for the entire coupling regime, thus facilitating the analysis on the transition [26]. The polaron picture has also been effectively applied in extracting various patterns of symmetry breaking [36] in non-linear couplings [35, 36, 71], understanding the topological transitions [37–39], and comprehending the interference fringes in the Wigner function and the hidden squeezing transition [38]. The polaron picture includes polarons with displacement and frequency renormalization which capture the main physics in the

* yingzj@lzu.edu.cn

QPT [4, 26, 30, 31, 33, 35–39, 44, 70, 71]. However, the considered polarons are symmetric, while the subtle energy competitions may deform the polarons and lead to asymmetry. A detailed analysis on such a missing physics is lacking.

In this work, we propose a variational method of asymmetric polaron picture which incorporates the missing polaron asymmetry degree of freedom. The method not only leads to a higher accuracy than the previous symmetric polaron picture but also reveals more physics that was not captured in the symmetric polaron picture. Indeed, we find that in the ground state both the polarons and antipolarons are asymmetrically deformed to a large extent in the entire coupling regime, which reflects the attracting of the polaron and antipolaron in the ground state. Such an asymmetry reaches a maximum around the QPT. We also find an emerging transition of imbalance reversal for the asymmetry extent of the polarons and the antipolarons. We also analyze the first excited state in which we find asymmetry direction transition for the polarons, which reflects a repelling tendency of the polarons and the antipolarons oppositely to the ground state. Finally, we apply the method for quantum Fisher information analysis and critical coupling extraction, with the improvements over the symmetric polaron picture. Our results reveal more underlying physics from the subtle energy competitions in light-matter interactions, with potential for broader applications.

The paper is organized as follows. Section II introduces the QRM with the transform to the position space. Section III presents our variational method in the asymmetric polaron picture and shows the improved accuracy. Section IV shows the features, transitions and the phase diagram of the ground state extracted by the asymmetric polaron picture. Section V analyzes the behavior of the first excited state and the phase diagram with additional transitions of polaron asymmetry. Section VI applies the method and shows the improvements in quantum Fisher information and critical couplings. Section VII summarizes the conclusions.

II. MODEL AND SYMMETRY

The QRM [22–24] is a most fundamental model for light-matter interactions, describing the coupling of a two-level system (qubit) with a single-mode light field. Under the rotating-wave approximation it is equivalent to the Jaynes-Cummings model [105, 119]. The QRM and its extensions also have a broad relevance, being a fundamental building block for quantum information and quantum computation [7, 123–126], applied in quantum metrology [30–33, 43, 54–68], bridged to many-body systems [29, 34], connected to models in condensed matter [8] and couplings in nanowires [127–131] and cold atoms [132–135]. The Hamiltonian of the standard QRM

reads

$$H_R = \omega \hat{a}^\dagger \hat{a} + \frac{\Omega}{2} \sigma_x + g \sigma_z (\hat{a}^\dagger + \hat{a}) \quad (1)$$

where $\hat{a}^\dagger (\hat{a})$ is the bosonic creation (annihilation) operator for the light field with frequency ω . The two-level system is represented by the Pauli matrices $\sigma_{x,y,z}$ with Ω being the level splitting. The coupling strength is denoted by g . In recent years, ultra-strong [5–19, 21] and deep-strong [17, 19, 118] couplings have been realized in superconducting circuit systems. Here, the adopted spin notation as in Refs.[26, 80] which conveniently represents the two flux states in the flux-qubit circuit systems [136] by $\sigma_z = \pm$. One can exchange σ_x and σ_z to retrieve the conventional form of the QRM by a spin rotation around the axis $\vec{x} + \vec{z}$.

By the transform $\hat{a}^\dagger = (\hat{x} - i\hat{p})/\sqrt{2}$, $\hat{a} = (\hat{x} + i\hat{p})/\sqrt{2}$, where $\hat{x} = x$ and $\hat{p} = -i\frac{\partial}{\partial x}$, the Hamiltonian can be mapped onto the position space and rewritten as

$$H = \sum_{\sigma_z=\pm} \left(h^{\sigma_z} |\sigma_z\rangle \langle \sigma_z| + \frac{\Omega}{2} |\sigma_z\rangle \langle \bar{\sigma}_z| \right) + \varepsilon_0. \quad (2)$$

Here $\bar{\sigma}_z = -\sigma_z$ and $h^\pm = \frac{1}{2}\omega(\hat{p}^2 + v_\pm)$ is an effective single-particle energy in a spin-dependent harmonic-oscillator potential $v_\pm = (\hat{x} \pm g')^2$ with a potential displacement $g' = \sqrt{2}g/\omega$, while $\varepsilon_0 = -\frac{1}{2}\omega(g'^2 + 1)$ is a constant energy. Now on the σ_z basis Ω becomes the strength of tunneling in the position space or spin flipping in the spin space [26, 80].

The model has parity symmetry, $[\mathcal{P}, H] = 0$, where the parity operator $\mathcal{P} = \sigma_x(-1)^{\hat{a}^\dagger \hat{a}}$ contains simultaneous spin reversal $\pm \rightarrow \mp$ and space inversion $x \rightarrow -x$ [36]. Therefore, the wave function takes the form $|\Psi\rangle = \frac{1}{\sqrt{2}}(|\psi_+\rangle \otimes |\uparrow\rangle + |\psi_-\rangle \otimes |\downarrow\rangle)$ where

$$\psi_+(x) = \psi(x), \quad \psi_-(x) = P\psi(-x). \quad (3)$$

Here the spin-up \uparrow (spin-down \downarrow) label is an alternative representation for state $\sigma_z = + (-)$ and $P = 1 (-1)$ corresponds to positive (negative) parity. The ground state has a negative parity which gains a negative tunneling energy, being more favorable to lower the energy.

III. ASYMMETRIC POLARON PICTURE

We shall first analyze the physical picture in the QPT of the QRM. With the extracted physical ingredients that play roles in the QPT, we propose the variational method in asymmetric polaron picture.

A. Physics in asymmetric polaron picture

Potential displacements: In the absence of coupling the potential $v_\pm \rightarrow x^2$ is simply a harmonic-oscillator potential and each spin components of the ground state is a

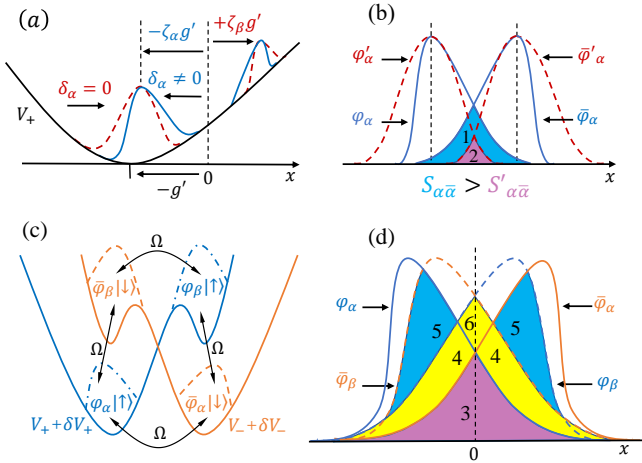


FIG. 1. *Schematic diagram for asymmetric polaron picture.* (a) Polarons labeled by α (antipolarons labeled by β) with displacement $-\zeta_\alpha g'$ ($+\zeta_\beta g'$) renormalized from the potential displacement $-g'$ of v_+ (parabolic line). Symmetric (Asymmetric) polaron and antipolaron in dashed (solid) lines have an asymmetric factor $\delta_i = 0$ ($\delta_i \neq 0$) where $i = \alpha, \beta$. (b) Enlarged overlap for asymmetric wave packets (solid) relative to symmetric ones (dashed). The overline over φ denotes spin-down (- or \downarrow) component. (c) Four channels of tunneling between spin-up (+ or \uparrow) and spin-down components of polarons and antipolarons accommodated in effective potentials $v_\pm + \delta v_\pm$. (d) Different overlaps among farther asymmetric polarons and closer asymmetric antipolarons due to potential difference in (a).

Gaussian wave packet in the lowest state ϕ_0 of quantum harmonic oscillator. When the coupling is turned on, the potentials v_\pm of the two spin components are separated and shift in opposite directions with displacements $x_0^\pm = \mp g'$. In Fig. 1(a) the potential v_+ is plotted as the parabolic curve with the displacement represented by the bottom position at $x_0^+ = -g'$ which is shifting to the left side of the origin (marked by the vertical dashed line at $x = 0$). A reflection with respect to the origin will give the potential v_- .

Wave-packet displacements and polarons: Accordingly the wave packet in each spin component has a tendency to follow the potential in the displacement. However, the tunneling tends to prevent the displacement of the wave packets as remaining unmoved around the origin $x = 0$ would have a maximized wave-packet overlap between the two spin components to gain more negative tunneling energy for the ground state. A larger coupling will lead to larger potential displacement thus a higher potential cost for the wave packets to stay around the origin, and finally the wave packets will also move away from the origin but with a discount of the potential displacement, $\zeta_\alpha g'$, to partially keep the tunneling energy. The discounted wave-packet displacement is shown in Fig. 1(a) by the other vertical line at $x_\alpha^+ = -\zeta_\alpha g'$ which marks the peak position of the moving wave packet in the dashed curve. Correspondingly the wave packet in the spin-down com-

ponent is located around $x_\alpha^- = -\zeta_\alpha g'$ due to the parity symmetry. These wave packets with displacements in the same direction of the potentials represent the so-called polarons [26, 69]. The term of “polaron” is borrowed from condensed matter in the sense that a displaced spin state is accompanied with a finite number of photons as in a coherent state, which is analogous to the electron surrounded by a phonon cloud due to the atom deviation from the lattice site. Here we denote the polarons by φ_α for spin-up component and $\bar{\varphi}_\alpha(x)$ for spin-down component.

Induced wave packets and antipolarons: On the other hand, the tunneling will induce another kind of wave packets with the displacements $x_\beta^\pm = \pm \zeta_\beta g'$ in the two spin components but on the other sides of the origin that are actually overlapping with the opposite-spin wave packets at $x_\alpha^\pm = \mp \zeta_\alpha g'$. Indeed, the eigen equation can be rewritten as $\frac{1}{2}\omega(\hat{p}^2 + v_\pm + \delta v_\pm)\psi_\pm(x) = E\psi_\pm(x)$ where

$$\delta v_\pm = \frac{\Omega}{\omega}\psi_\mp(x)/\psi_\pm(x) \quad (4)$$

is an induced effective potential in addition to the bare potential v_\pm . This induced potential will create a potential well which accommodates a secondary wave packet, as sketched in Fig. 1(c). We also plot this secondary wave packet over the bar potential for spin-up component in Fig. 1(a) in dashed curve. These secondary wave packets represent antipolarons in the sense that their displacements are in the opposite directions of the potentials. Here we denote the antipolarons by $\varphi_\beta(x)$ for the spin-up component and $\bar{\varphi}_\beta(x)$ for the spin-down component.

Wave-packet overlap and frequency renormalization: The polarons and antipolarons form four channels of tunneling, as indicated by the double-headed arrows in Fig. 1(c), between polarons on the same sides and between polarons and antipolarons on the opposite sides. The tunneling strength is decided by the overlaps of the polarons and antipolarons, as illustrated by the region 2 in Fig. 1(b). To gain more tunneling energy the wave packet will be extended to expand the overlap region. Effectively this wave-packet extension can be described by a frequency renormalization $\omega \rightarrow \xi_i \omega$ with $i = \alpha, \beta$ depending on the polarons and antipolarons.

Potential height and polaron weight: As one sees in Fig. 1(a) the antipolarons have a higher potential than the polarons, which leads to a weight difference. We denote the weight of the polarons by α and that of the antipolarons by β in the wave-packet superposition. Generally the antipolarons have a smaller weight than the antipolarons, $\beta < \alpha$. Counter-intuitively a larger antipolaron weight can still occur as will be addressed in the discussion later on.

Asymmetric deformation and its origins: Note both the polarons and the antipolarons so far are symmetric with respect to their peak position as in the Gaussian wave packet in ϕ_0 . However, the right and left sides of either a polaron or an antipolaron actually have different potential values as one may notice in Fig. 1(a),

which would lead to an imbalance of density distribution on the two sides as sketched by the solid-line wave-packets in contrast to the dashed-line symmetric ones in Fig. 1(a). Moreover, the left-right-side tunneling are dominantly determined by the overlapping sides of a polaron and an antipolaron, the wave-packet density on the overlapping sides around the origin has the leading impact on the tunneling energy relatively to the other sides farther away from the origin. This side difference in tunneling contribution also results in asymmetric deformation. In Fig. 1(b) we compare the asymmetric polarons and antipolarons (solid curves) and the symmetric ones (dashed curves), which shows the asymmetric ones have a wider overlapping region (marked by 1) than that of the symmetric ones (marked by 2).

B. Variational method in asymmetric polaron picture

Based on the above analysis, we propose a trial variational wave function which takes into account all the key physical ingredients in the asymmetric polaron picture, via a linear combination of the polaron and the antipolaron

$$\psi(x) = \alpha\varphi_\alpha(x) + \beta\varphi_\beta(x). \quad (5)$$

Here, besides the polaron weights α and β , the wave packets $\varphi_\alpha(x)$ and $\varphi_\beta(x)$ contain the displacement discount factor $\zeta_{\alpha,\beta}$, the frequency renormalization $\xi_{\alpha,\beta}$, and the asymmetric factor $A_{\alpha,\beta}$

$$\varphi_\alpha(x) = (1 + A_\alpha)\phi_0(\xi_\alpha, x + \zeta_\alpha g'), \quad (6)$$

$$\varphi_\beta(x) = (1 + A_\beta)\phi_0(\xi_\beta, x - \zeta_\beta g'), \quad (7)$$

where

$$\phi_0(x) = \left(\frac{\xi}{\pi}\right)^{1/4} \exp\left[-\frac{1}{2}\xi x^2\right] \quad (8)$$

is the ground state of quantum harmonic oscillator with frequency ξ . Although the asymmetric factor may have a more general form, in the principle of choosing the simplest form to capture the dominant physics, we take a linear asymmetric order of asymmetric

$$A_\alpha = \delta_\alpha x_\alpha + \mathcal{O}(x_\alpha^3), \quad A_\beta = \delta_\beta x_\beta + \mathcal{O}(x_\beta^3), \quad (9)$$

where $x_\alpha = x + \zeta_\alpha g'$ and $x_\beta = x - \zeta_\beta g'$ denote the distances from the symmetric polaron and antipolaron positions. The adoption of (9) is also based on the fact that the leading contribution is coming from the region close to the wave-packet peak, where the linear order plays the key role, while it is exponentially decaying and vanishing away from the peak. The even-order terms are symmetric, the effect of which has been encoded in the frequency renormalization, thus unnecessary to re-include here.

The variational energy can be obtained as

$$E = h_{++}^+ + \frac{1}{2}P\Omega n_{+-} + \varepsilon_0 \quad (10)$$

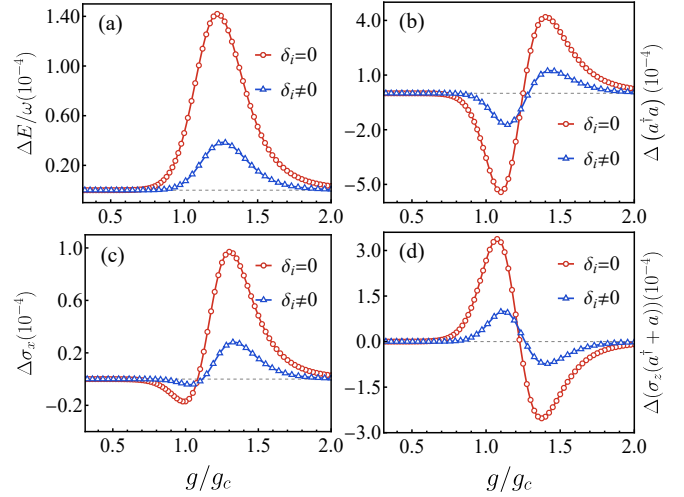


FIG. 2. Accuracy improvements in the asymmetric polaron picture. The discrepancy $\Delta q = q_{var} - q_{ED}$ of variational physical quantities q_{var} from the results of exact diagonalization (ED) for q being (a) the total energy E , (b) the photon number $\langle a^\dagger a \rangle$, (c) the spin expectation $\langle \sigma_x \rangle$, (d) the coupling correlation $\langle \sigma_z(a^\dagger + a) \rangle$. The circles (triangles) represent the symmetric (asymmetric) case with $\delta_i = 0$ ($\delta_i \neq 0$), where $i = \alpha, \beta$, illustrated for the first excited state at $\omega = 0.15\Omega$.

where $h_{++}^+ = \langle \psi | h^+ | \psi \rangle$ and $n_{+-} = \langle \psi | \bar{\psi} \rangle$ with $\bar{\psi}(x) = \psi(-x)$. The variational parameters $\{\alpha, \beta, \zeta_\alpha, \zeta_\beta, \xi_\alpha, \xi_\beta, \delta_\alpha, \delta_\beta\}$ are optimized by energy minimization subject to the normalization condition $\langle \psi | \psi \rangle = 1$. We leave the detailed explicit expressions in Appendix B.

C. High accuracy of variational method in asymmetric polaron picture

For the QRM the ground state is the lowest state of all eigenstates including both negative and positive parities, while the first excited state is the lowest state of all eigenstates with positive parity. The accuracy for the ground state in the symmetric polaron picture has been addressed for both numerical calculations [26, 44, 70] and analytic analysis [26, 35–39, 44]. Here our improved variational method in asymmetric polaron picture is valid for both the ground state and the first excited state. Fig. 2 shows the discrepancy from the result of exact diagonalization (ED) [36, 40] of several physical quantities of the first excited state, including the energy E , the mean photon number $\langle a^\dagger a \rangle$, the tunneling or spin-flipping strength $\langle \sigma_x \rangle$, and coupling correlation $\langle \sigma_z(a^\dagger + a) \rangle$. Here the discrepancy of a quantity q is defined by $\Delta q = q_{var} - q_{ED}$, where q_{var} is variational result and q_{ED} is the ED result. In all panels of Fig. 2 the circles are the outcome of symmetric polaron picture ($\delta_i = 0$) and the triangles are that of asymmetric polaron picture ($\delta_i \neq 0$). One sees that the discrepancy is substantially reduced in the asymmetric polaron picture relatively to the results of the symmetric polaron picture. The accuracy improvement

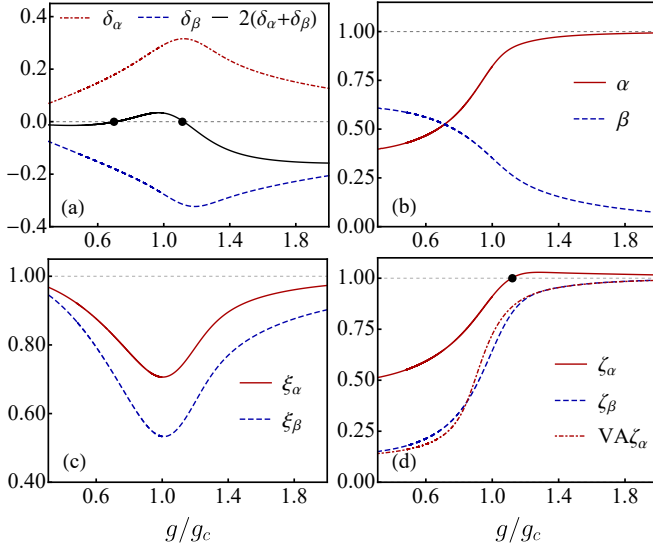


FIG. 3. *Variational parameters and transitions in the ground state.* Evolution of the variational parameters for (a) asymmetry factors δ_α (dot-dashed), δ_β (dashed), $\delta_\alpha + \delta_\beta$ (solid), (b) weights of polaron (α , solid) and antipolaron (β , dashed), (c) renormalization factors of polaron (ξ_α , solid) and antipolaron (ξ_β , dashed), (d) displacement renormalization factors of polaron (ζ_α , solid) and antipolaron (ζ_β , dashed). The dot-dashed line is the asymmetric polaron displacement $\zeta_\alpha + \zeta_\beta$ from Eq. (17). Here $\omega = 0.15\Omega$.

is similar for the ground state. The accuracy guarantees that an analysis in the asymmetric polaron picture is reliable. In the next sections we will apply the asymmetric polaron picture to extract the underlying physics in connection with the PQTs missed by the symmetric polaron picture.

IV. POLARON ASYMMETRY AND TRANSITIONS IN THE GROUND STATE

Tracking the evolution of the variational parameters in the variation of the coupling strength will reveal some underlying physics in the ground state. Indeed, we observe several transition-like features and try to clarify the mechanisms, as addressed below.

A. Transition at maximum frequency renormalization

The frequency renormalization factors ξ_α and ξ_β are shown in Fig. 3(c). One sees that both ξ_α and ξ_β are smaller than 1, which means that the distributions of the wave packets are more extended than the initial wave function ϕ_0 in the absence of coupling. As addressed in Sec. III A such an wave-packet extension enlarges the wave-packet overlap, thus gaining more tunneling energy which is negative in the ground state. The appearance

of the antipolarons effectively is a precess of wave-packet splitting [26, 80] in which the energy competition between the tunneling and the potential is going beyond a limit of balance. Around the point of breaking the balance the wave-packet extension reaches a maximum extent. A transition-like variation occurs once the wave packets finally split.

The wave-packet splitting occurs around the critical coupling scale [26]

$$g_c = \sqrt{\omega^2 + \sqrt{\omega^4 + g_{c0}^4}} \quad (11)$$

which is shifting with finite frequency away from the critical point [25]

$$g_{c0} = \frac{\sqrt{\omega\Omega}}{2}. \quad (12)$$

Eq. (12) can be obtained in a semiclassical consideration in which the spin is kept as the quantum part while the space part takes the classical approximation by a mass point moving in the classical potential [35, 36]. Such a semiclassical approximation is valid in the low-frequency limit, $\omega/\Omega \rightarrow 0$, while Eq. (11) works for finite frequencies as the space part is also based on a quantum-mechanics consideration with wave function in wave packets rather than a classical mass point.

Still, Eq. (11) only includes the displacement part in the wave-packet splitting, while further taking into the effect of frequency renormalization leads to a more accurate expression in a fractional-power form [44]

$$g_c^F = g_{c0} \left[1 + \frac{1}{100\alpha_{FS}} \left(\frac{\omega}{\Omega} \right)^{2/3} - \frac{1}{8} \left(\frac{\omega}{\Omega} \right)^{4/3} \right], \quad (13)$$

where $\alpha_{FS} = 1/137$, as extracted from the peak position of the QFI. Expression (13) is accurate in $\omega/\Omega \in [0, 0.5]$ regime, while a higher-order fitting

$$g_c^F = g_{c0} \left[1 + c_1 \left(\frac{\omega}{\Omega} \right)^{2/3} + c_2 \left(\frac{\omega}{\Omega} \right)^{4/3} + c_3 \left(\frac{\omega}{\Omega} \right)^{6/3} \right], \quad (14)$$

where $c_1 = 1.3715$, $c_2 = -0.1311$, $c_3 = 0.0184$ can extend the validity to the entire frequency regime $\omega/\Omega \in [0, 3]$. Such a fractional-power form comes from the effect of frequency renormalization, in contrast to the less-accurate integer-power form without frequency renormalization [44].

B. Transition of polaron weight reversal

Fig. 3(b) shows a transition of polaron weight reversal. In a large coupling g the antipolarons have a smaller weight (β) than that of the polarons (α) due to the higher antipolaron potential. However, this weight imbalance can be reversed at a small coupling, especially at low frequencies, yielding overweighted antipolarons in the sense that they counter-intuitively have a larger weight than

the polarons. In fact, as indicated by the smaller values of ζ_β in Fig. 3(d), the higher antipolaron potential also leads to a closer distance between the antipolarons in the two spin components than the polarons. This yields a larger antipolaron wave-packet overlap than the polarons, as indicated by Fig. 1(d) where the antipolaron overlap (regions 3,4,6) has an extra part than the that of the polaron (region 4), which makes a larger weight of antipolarons more favorable to gain more tunneling energy. At low frequencies, the potential is more flat so that the overweighted polarons have less potential cost. As a consequence, the transition of the polaron weight reversal occurs.

C. Considerable asymmetry strength and asymmetry sign

Fig. 3(a) illustrates the behavior of the asymmetry parameters δ_α for the polarons (long-dashed) and δ_β for the antipolarons (short-dashed). The first features we observe are the asymmetry strength and asymmetry sign. Indeed, the asymmetry is quite considerable for both the polarons and the antipolarons in the entire coupling regime, as demonstrated by the finite values of δ_α and δ_β . This means that the asymmetry effect is fairly strong and our consideration in asymmetric polaron picture is necessary. Furthermore, δ_α and δ_β have opposite signs, with the former being positive while the latter being negative, indicating that $\varphi_\alpha(x)$ has more probability on its right side than its left side while it is reverse for $\varphi_\beta(x)$. This means that it is really the wave-packet sides close to the origin that have a larger density, which increases the overlaps between left and right wave packets, as aforementioned for Fig. 1(b). This enlarged overlap not only gains more negative tunneling energy, but also reduces the potential energy.

D. Reversals of asymmetry imbalance

A closer look at the competition of δ_α and δ_β brings our attention to the asymmetry imbalance and an underlying transition of asymmetry imbalance reversal. Indeed, as shown in Fig. 3(a) at a large coupling the magnitude of δ_β is larger than that of δ_α , which comes from the steeper potential of the antipolarons than that of the polarons as in Fig. 1(a). However, when the coupling strength is reduced, this asymmetry imbalance is reversed around $g = 1.12g_c$ (marked by the dot). This reversal arises from the subtle competitions between the potential difference and the tunneling energy: (i) First, at a reduced coupling strength the potential of the antipolarons is less steep, which decreases the potential difference from the polarons. (ii) Second, the antipolarons and the polarons are getting closer so that left-right-side tunneling energy becomes more dominant over the potential gradient difference, due to the enlarged antipolaron-polaron over-

lap as sketched by the regions 3,4,6 in Fig. 1(d). Note here the left-right polarons have larger distance than the left-right antipolarons so that the polarons need a larger asymmetry to gain left-right tunneling as much as possible. (iii) Third, besides the left-right channels of tunneling there are also same-side tunneling, a larger polaron asymmetry will enhance the same-side overlap (regions 3,4,5 in Fig. 1(d)) between the antipolarons and the polarons. These competing factors together lead to the first reversal asymmetry imbalance.

When the coupling is reduced further one sees another reversal of the asymmetry imbalance around $g = 0.71g_c$ in Fig. 3(a) (marked by the other dot). In fact, in such a small- g regime, all the polarons and antipolarons are very close and nearly in full overlapping. In such a situation, the competition mainly lies between the left-right tunneling (ii) and the same-side tunneling (iii), which depends on the difference of the wave-packet overlap region 5 and region 6. Actually, with the nearly full overlapping, the variation of region 5 is coming from the peak part which is less sensitive to the asymmetry changes than the variation of region 6 from the faster-varying wave-packet sides. A larger δ_β can get a relatively easier increase of tunneling, which leads to the slightly larger magnitude of δ_β again.

E. Unnormal displacement renormalization in attractive polarons and antipolarons

Fig. 3(d) gives the evolution of the displacement renormalization factors ζ_α and ζ_β . A general tendency is that ζ_α and ζ_β are small before g_c but approach to be 1 after g_c , which reflects the process of wave packet splitting process for the QPT, in the picture that the polarons and antipolarons tend to stay around the origin before the transition and start to follow the displacements of the potentials after the transition. Such a transition-like process is abrupt in the low-frequency limit and softened at finite frequencies due to the wave-packet broadening [26]. Normally the values of ζ_α and ζ_β should be both smaller than 1. However, in Fig. 3(d) we see at a large coupling regime, ζ_α unnormally goes beyond the normal limit value of 1.

This unnormal behavior of ζ_α originates from the strong asymmetric effect. In fact, not only the ζ_α can directly renormalizes the polaron displacement, but also the polaron asymmetry can indirectly affect the peak position of the polarons due to the asymmetry-induced wave-packet deformation. Indeed, the final peak positions of $\varphi_\alpha(x)$ and $\varphi_\beta(x)$ are located at

$$x_i^p = \eta_i \zeta_i g' + \frac{\sqrt{\xi_i + 4\delta_i^2} - \sqrt{\xi_i}}{2\delta_i \sqrt{\xi_i}} \quad (15)$$

where $i = \alpha, \beta$, $\eta_\alpha = -1$ and $\eta_\beta = 1$. The first term of Eq. (15) is the original renormalized displacement, while second term stems from the polaron asymmetry. We can

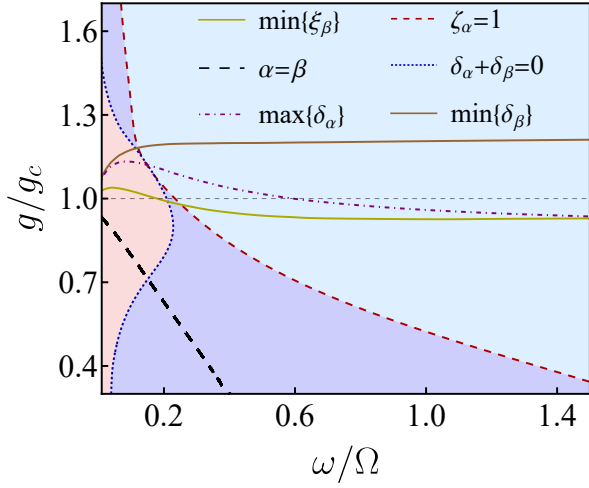


FIG. 4. *Ground-state phase diagram in the ω - g plane.* The dark-yellow (light gray) solid line denotes the transition around g_c (11) as reflected by the maximum of ξ_β . The brown (dark gray) solid line around $g = 1.2g_c$ (the dot-dashed line) labeled by $\text{Min}\delta_\beta$ ($\text{Max}\delta_\alpha$) is the maximum asymmetry point of the antipolaron (polaron). The dotted boundary marks the reversal of asymmetry imbalance, with $\delta_\alpha + \delta_\beta > 0$ inside the boundary and $\delta_\alpha + \delta_\beta > 0$ outside. The dashed line separates the $\zeta_\alpha > 0$ region above the line and the $\zeta_\alpha < 0$ region below the line. The long-dashed slash is the boundary $\alpha = \beta$ for weight reversal with $\alpha > \beta$ above the boundary and $\alpha < \beta$ below.

introduce an effective displacement renormalization ζ_i^p to rewrite the final peak position as

$$x_i^p \equiv \eta_i \zeta_i^p g' = \eta_i (\zeta_i + \zeta_i^\delta) g', \quad (16)$$

with an asymmetry-induced effective renormalization factor

$$\zeta_i^\delta = \eta_i (\sqrt{\xi_i + 4\delta_i^2} - \sqrt{\xi_i}) / (2\delta_i \sqrt{\xi_i} g'). \quad (17)$$

Note that δ_i has a sign opposite to η_i and the asymmetry contributes to discount the displacement. In the large-coupling regime the polarons have a weight dominant over the antipolaron due to the enlarged potential difference, in this situation the polarons tend to stay nearly at the potential bottom, with a weak displacement renormalization. However, the strong asymmetry creates a relatively large displacement discount which excessively takes the role of the displacement renormalization. As a result, the original renormalization ζ_α has to oppositely expand to partially cancel the overflow of the strong-asymmetry-induced displacement discount, which leads to a ζ_α larger than 1. Although this unnormal ζ_α does not represent the final peak position, it is a sign that reflects a strong asymmetry effect relatively to the original displacement renormalization.

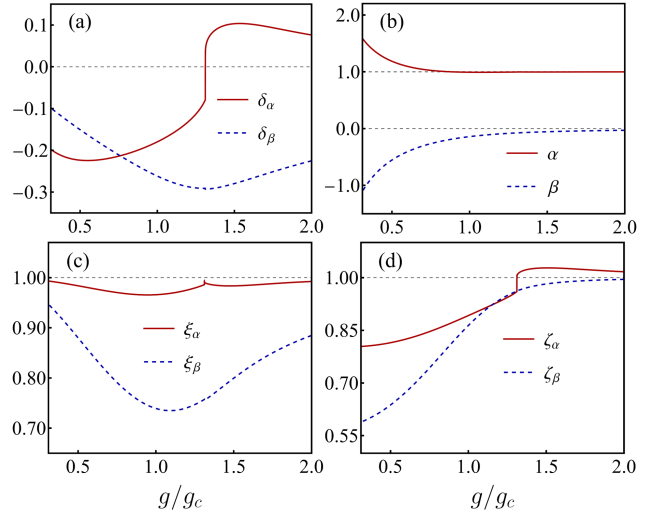


FIG. 5. *Variational parameters and transitions in the first excited state.* Evolution of the variational parameters for (a) asymmetry factors δ_α (solid) and δ_β (dashed), (b) weights of polaron (α , solid) and antipolaron (β , dashed), (c) renormalization factors of polaron (ξ_α , solid) and antipolaron (ξ_β , dashed), (d) displacement renormalization factors of polaron (ζ_α , solid) and antipolaron (ζ_β , dashed). Here $\omega = 0.5\Omega$.

F. Ground-state phase diagram in asymmetric polaron picture

The ground-state phase diagram is presented in Fig. 4 in the ω - g plane. The horizontal straight dashed line marks the transition coupling scale g_c [Eq.(11)] at finite frequencies [26], while the dark-yellow (light gray) solid line around $g = g_c$ represents the minimum point of antipolaron frequency renormalization ξ_β which reflects the transition-like behavior. The long-dashed slash denotes the boundary $\alpha = \beta$ for the polaron weight reversal. Besides these transitions which are the same as in the symmetric polaron picture, some additional boundaries emerge in the asymmetric polaron picture: The brown (dark gray) solid line around $g = 1.2g_c$ is the minimum point of asymmetry factor δ_β of the antipolarons, while the dot-dashed line labels the maximum point of δ_α of the polarons. The dotted curve marks the boundary for the asymmetry imbalance reversal, which occurs at low frequencies as the flat potential at low frequencies fulfills the condition of less steep potential (i) in Sec. IV D. The short-dashed curve is the boundary $\zeta_\alpha = 1$ for the unnormal displacement renormalization. The phase diagram provides an overall view for the subtle energy competitions in the ground state and abundant physics explored by the asymmetric polaron picture.

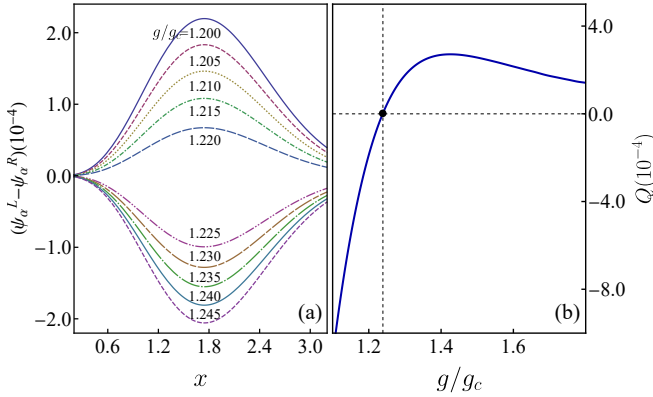


FIG. 6. Transition of asymmetry sign reversal confirmed by the ED results for the first excited state. (a) Asymmetry of polaron wave packet by difference between its left side (ψ_α^L) and right side (ψ_α^R) as a function of the distance x from the peak, at couplings around the point of asymmetry sign reversal. The numbers give the coupling strength g/g_c . Here ψ_α is extracted by polaron fitting of the ED wave function. (b) The sign reversal of the asymmetry quantity Q (Eq.(18)) from the ED wave function. Here $\omega = 0.5\Omega$.

V. THE FIRST EXCITED STATE IN ASYMMETRIC POLARON PICTURE

Now we apply the variational method of asymmetric polaron picture to study the first excited state. We will see that the first excited state manifests some transitions and physics differently from the ground state.

A. Opposite weight signs of polarons and antipolarons

Fig. 5(b) shows the weights of the polarons and antipolarons. At a first glance one can immediately see the first difference from the ground state that the weights of the polarons and the antipolarons here have opposite signs, as β turns to be negative. This comes from the parity difference, as the ground state has a negative parity $P = -1$ while the first excited state possesses a positive parity $P = +1$. Although the energy is higher than the ground state, the first excited state is the lowest state within all the states in positive parity. Under the positive parity, the opposite signs of the polarons and antipolarons guarantee a negative tunneling energy in the same-side channels $\Omega_{\alpha\beta} = \frac{\Omega}{2}\alpha\beta P\langle\varphi_\alpha(x)|\bar{\varphi}_\beta(x)\rangle$ and $\Omega_{\alpha\beta} = \frac{\Omega}{2}\alpha\beta P\langle\bar{\varphi}_\beta(x)|\varphi_\alpha(x)\rangle$, despite that the left-right channels, $\Omega_{\alpha\alpha} = \frac{\Omega}{2}\alpha^2 P\langle\varphi_\alpha(x)|\bar{\varphi}_\alpha(x)\rangle$ and $\Omega_{\beta\beta} = \frac{\Omega}{2}\beta^2 P\langle\bar{\varphi}_\beta(x)|\varphi_\beta(x)\rangle$, have a positive tunneling energy which however has a smaller contribution than the same-side channels due to the smaller wave-packet overlaps $\langle\varphi_\alpha(x)|\bar{\varphi}_\alpha(x)\rangle$ and $\langle\bar{\varphi}_\beta(x)|\varphi_\beta(x)\rangle$.

B. Weight magnitudes both increasing for polarons and antipolarons in reduced coupling

With a further observation on the weight evolution one may realize that, when the coupling strength is reduced, the weight magnitudes of the polarons and the antipolarons, $|\alpha|$ and $|\beta|$, are both increasing (subject to the normalization). In contrast, in the ground state the polaron weight is decreasing while antipolaron weight is increasing, so that α and β have a similar amplitude at small values of g . This special weight magnitude behavior comes from the parity difference. as the wave-function normalization requires $\langle\psi|\psi\rangle = \alpha^2\langle\varphi_\alpha(x)|\varphi_\alpha(x)\rangle + \beta^2\langle\varphi_\beta(x)|\varphi_\beta(x)\rangle - P|\alpha\beta|\langle\varphi_\alpha(x)|\varphi_\beta(x)\rangle = 1$. We know that a smaller coupling leads to a larger overlap $\langle\varphi_\alpha(x)|\varphi_\beta(x)\rangle$ in a closer polaron-antipolaron distance and an increasing antipolaron weight $|\beta|$ in a lower potential, while the same-side overlaps $\langle\varphi_\alpha(x)|\varphi_\alpha(x)\rangle$ and $\langle\varphi_\beta(x)|\varphi_\beta(x)\rangle$ are much less affected by the left-right distance and the left-right potential difference. In such a situation, the ground state with $P = -1$ needs a decreasing polaron weight $|\beta|$ to fulfill the normalization condition, while this trend is reversed for the first excited state with $P = +1$ due to the third term of $\langle\psi|\psi\rangle$ now becomes negatively increasing. Therefore, we have increasing weight magnitudes for both polarons and antipolarons.

C. Transition of polaron attraction and repulsion

In the first excited state the transition around g_c reflected by maximum frequency renormalization (minima of ξ_α and ξ_β) is similar to the ground state, as illustrated by Fig. 5(c). A transition different from the ground state arises as the asymmetry factor δ_α changes sign at a certain point when the coupling is reduced, as shown in Fig. 5(a). Note that the sign reversal in Sec. IV D for the ground state is for the imbalance between two asymmetry factors δ_α and δ_β , while here the sign reversal occurs in one asymmetry factor δ_α . The δ_α sign shifting from positive to negative means that some distribution probability of the polarons are moved from the sides close to the origin to the opposite sides far away from the origin. This effect appears to be a change from attraction to repulsion. Indeed, the left and right polarons have a trend to avoid overlapping due to the positive tunneling energy of $\Omega_{\alpha\alpha}$ which is increasing due to the enlarged left-right polaron overlap $\langle\varphi_\alpha(x)|\bar{\varphi}_\alpha(x)\rangle$ in closer polaron distances when the coupling is reduced. The sign reversal of δ_α reduces $\langle\varphi_\alpha(x)|\bar{\varphi}_\alpha(x)\rangle$ to a largest degree. This sign transition does not happen to δ_β due to the potential-induced asymmetry is stronger in antipolarons.

The sign reversal of δ_α in the above is observed from the evolution of δ_α which is a variational parameter in energy minimization. This asymmetry transition might be further confirmed by results from exact diagonalization (ED). First, we use the variational wave function to

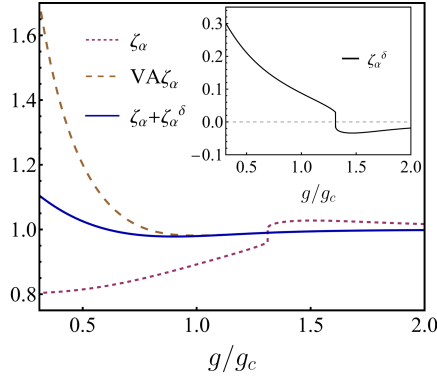


FIG. 7. *Transition of polaron attraction and repulsion in the first excited state.* The displacement factors from variational parameter ζ_α (dashed), from asymmetry ζ_α^d (Inset), and from the total one $\zeta_\alpha + \zeta_\alpha^d$ (solid), in the case of asymmetry reversal in Fig. 6.

fit the ED wave function, from which we can extract the asymmetry of the wavepacket, as indicated in Fig. 6(a) by the left-right difference around the main-peak position corresponding to the polaron. We see that indeed the left-right difference reverses the sign around the same transition point in Fig. 5(a).

To further verify this asymmetry reversal, we introduce an asymmetry quantity

$$Q = \int_{-\infty}^{\infty} \psi_{\text{ED}}^*(x) \text{sign}(x - x_m) e^{-(x-x_m)^2/2} \psi_{\text{ED}}(x) dx \quad (18)$$

where $\text{sign}(x)$ is the sign of x and x_m is the main-peak position of the ED wave function $\psi_{\text{ED}}(x)$. Here in the integrand the factor $e^{-(x-x_m)^2/2}$ filters the affection from the part far away from the peak, which corresponds to the antipolaron in the variational method, and amplifies contribution from the part around the peak, which corresponds to the polaron. The asymmetry is then captured by adding $\text{sign}(x - x_m)$ as a coefficient of $\psi_{\text{ED}}(x)$: Q would be canceled if $\psi_{\text{ED}}(x)$ is symmetric around the the peak, otherwise the sign of Q reflects different direction of asymmetry with higher density on the right side of the peak for $Q > 0$ and higher density on the left side for $Q < 0$. It turns out that there is really a sign reversal in Q as shown by Fig. 6(b), which occurs around the same point of the afore-mentioned asymmetry transition in δ_α sign reversal.

D. Polaron-density-cancellation-induced repulsion in positive parity

The polaron repulsive effect in Sec. V C is coming from the positive tunneling energy of $\Omega_{\alpha\alpha}$ in positive parity of the first excited state. The positive parity also leads to a “repulsion” effect from density cancellation. In fact the opposite signs of the weights α and β results in a

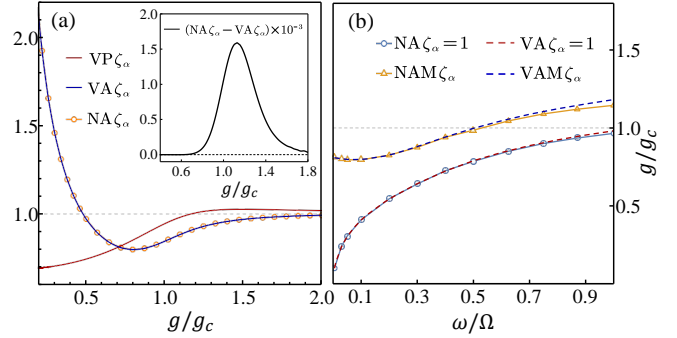


FIG. 8. *Polaron-density-cancellation-induced repulsion in the first excited state.* (a) Displacement factors of the main peak position by the numerically accurate wave function (NA ζ_α , circles) from the ED and by variational polaron fitting of the accurate ED wave function (VA ζ_α , solid line), at $\omega = 0.15\Omega$. The inset shows their discrepancy. (b) Frequency dependence of the increasing/decreasing turning point or minimum point (NAM ζ_α and VAM ζ_α , triangles and dashed line) and the point going beyond 1 (NA $\zeta_\alpha = 1$ and VA $\zeta_\alpha = 1$, circles and long-dashed line) in (a).

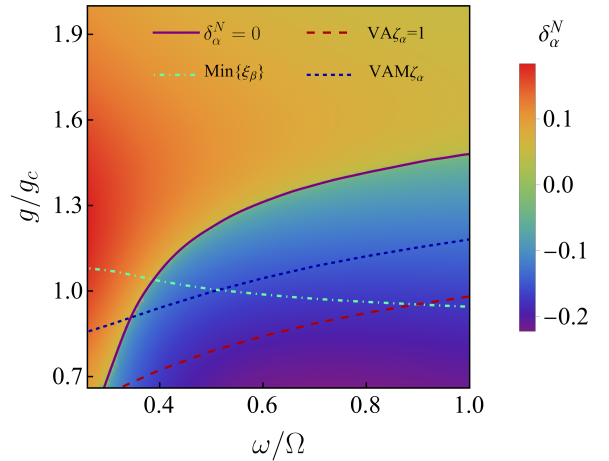


FIG. 9. *Phase diagram of the first excited state in the ω - g plane.* The dot-dashed line represents the transition around g_c , as reflected by the minimum of ξ_β . The density plot is for δ_α by polaron fitting of the numerical ED wave function (denoted by δ_α^N). The solid line marks the additional transition boundary for the sign reversal of δ_α . The dashed line and dotted line are the minimum point and the point going beyond 1 of main-peak ζ_α in Fig. 8(a).

wave-function cancellation in the meeting part of the polaron and the antipolaron, which reduces the density in the valley between the main polaron peak and the secondary antipolaron peak. Thus the polaron peak and the antipolaron peak are pushed farther away from each other, especially when they are close in the small couplings. This effect also appears to be repulsive-like.

Fig. 8(a) demonstrates the evolution of the final position of the main polaron peak by the line with circles,

the effective displacement renormalization factor ζ_α for which is turning from decreasing to increasing in coupling reduction and even becomes diverging at small couplings despite that the variational ζ_α (solid line without circles) is always decreasing and smaller than 1. Fig. 8(b) shows the frequency dependence of the increasing/decreasing turning point (triangles) of the final peak position and the point beyond 1 (circles). This “repulsion” effect is in a sharp contrast to the ground state where the polarons and antipolarons are attractive-like and their final peak position never goes beyond 1.

E. Phase diagram of the first excited state

Fig. 9 shows the phase diagram in the ω - g plane for the first excited state from the above discussions. The dot-dashed line represents the minimum point of ξ_β , which denotes the transition around g_c similar to the ground state. The density plot in Fig. 9 provides the map of δ_α numerically extracted (denoted by δ_α^N) from the fitting of the ED wave function illustrated in Fig. 6(a), with the sign reversal boundary (solid line) separating the positive (red, above the solid line) and negative (blue, below the solid line) regions. The transition of δ_α sign reversal is different from g_c , occurring below g_c at low frequencies and above g_c at high frequencies. The dashed line and the dotted line locate the increasing/decreasing turning point of the final main peak position and the point beyond 1 for the final peak displacement factor ζ_α , which reflects the degree of the effective polaron repulsion induced by the density cancellation in positive parity.

VI. APPLICATION IN QUANTUM FISHER INFORMATION

A. Quantum Fisher information (QFI) for quantum metrology

As established by the Cramér-Rao theorem [137] the measurement precision of experimental estimation on a parameter λ is bounded by $F_Q^{1/2}$ in quantum metrology. Here F_Q is the quantum Fisher information (QFI) defined as [137–139]

$$F_Q(\lambda) = 4 \left[\langle \psi'(\lambda) | \psi'(\lambda) \rangle - |\langle \psi'(\lambda) | \psi(\lambda) \rangle|^2 \right] \quad (19)$$

for a pure state $|\psi(\lambda)\rangle$ and ' denotes the derivative with respect to the parameter λ . A larger QFI would mean a higher precision accessible in measurements. For a real wave function $\psi(\lambda)$, as is usually the case in non-degenerate states of a real Hamiltonian, the second term in Eq. (19) vanishes so that the QFI can be simplified to be [44]

$$F_Q = 4 \langle \psi'(\lambda) | \psi'(\lambda) \rangle, \quad (20)$$

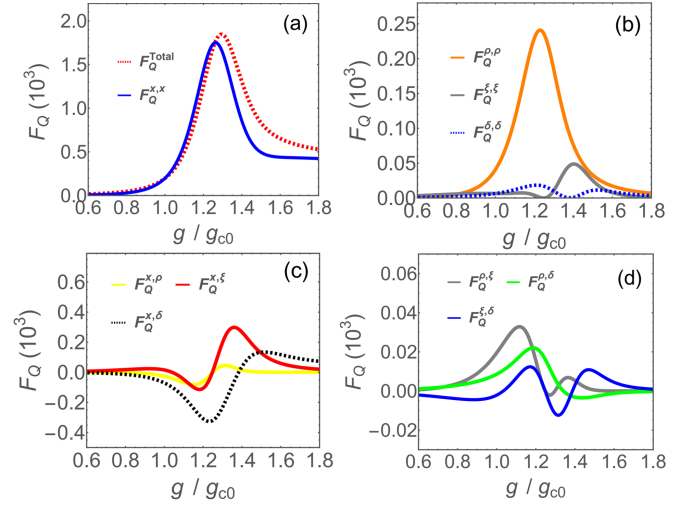


FIG. 10. *Decomposed quantum Fisher information (QFI) of the ground state and contribution of polaron asymmetry.* (a) The total QFI F_Q^{Total} (red dotted line) and the displacement part $F_Q^{x,x}$ (blue solid line). (b) Decomposed QFI from variations of polaron weight $[F_Q^{p,p}$, orange (light gray) solid line], frequency renormalization $[F_Q^{\xi,\xi}$, gray solid line] and polaron asymmetry $[F_Q^{\delta,\delta}$, blue dotted line]. (c) Interplay parts of QFI between displacement and polaron weight $[F_Q^{x,p}$, red (dark gray) solid line], frequency renormalization $[F_Q^{x,\xi}$, green (light gray) solid line] and polaron asymmetry $[F_Q^{x,\delta}$, black dotted line]. (d) Interplay parts of QFI between polaron weight and frequency renormalization $[F_Q^{p,\xi}$, gray solid line], polaron weight and asymmetry $[F_Q^{p,\delta}$, green (light gray) solid line] and frequency renormalization and asymmetry $[F_Q^{\xi,\delta}$, blue (dark gray) solid line]. Here $\omega/\Omega = 0.1$ and $g_{c0} = \sqrt{\omega\Omega}/2$ is the critical coupling in low-frequency limit.

which also applies for the ground state of the QRM (1) considered in the present work.

The appearance of QFI peak in QPTs can be employed for critical quantum metrology [30–33, 43, 54–68]. Conversely, such QFI peaks have been applied to identify the QPT in light-matter interactions [44]. In fact, the QFI is equivalent to the susceptibility of the fidelity. In an infinitesimal parameter variation $\delta\lambda$ the fidelity F can be expanded as

$$F = |\langle \psi(\lambda) | \psi(\lambda + \delta\lambda) \rangle| = 1 - \frac{\delta\lambda^2}{2} \chi_F, \quad (21)$$

so that the QFI corresponds to the susceptibility of the fidelity by $\chi_F = F_Q/4$ [31, 140–142]. The appearance of the QFI peak signals a QFT in fidelity theory [140–144].

In the following we shall apply the asymmetric polaron picture to analyze the QFI of the QRM.

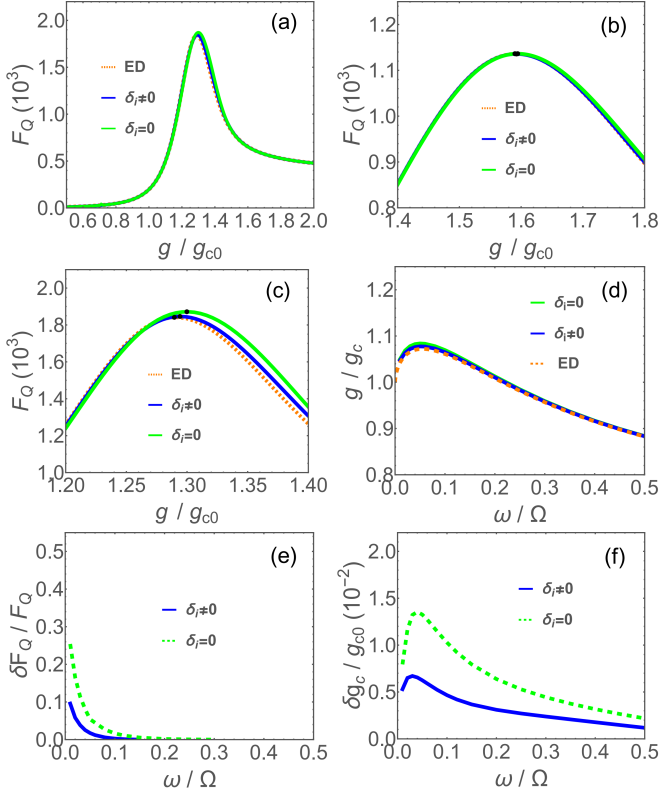


FIG. 11. *Improvements on QFI and critical coupling from polaron asymmetry.* (a) The QFI in symmetric ($\delta_i = 0$) and asymmetric ($\delta_i \neq 0$) polaron pictures compared to the exact diagonalization (ED) at $\omega/\Omega = 0.1$. (b) The QFI around the peak position at $\omega/\Omega = 0.3$. (c) Close-up view of the QFI around the peak position at $\omega/\Omega = 0.1$. (d) The critical couplings versus frequency extracted by the QFI peak position for the symmetric and asymmetric polaron pictures compared to the ED result in Eq. (14). (e) Discrepancy of the QFI peak values from the ED. (f) Discrepancy of the critical couplings from the ED.

B. Decomposed QFI and contribution of polaron asymmetry

In the asymmetric polaron picture, we have variation resources from displacement (x), frequency renormalization (ξ), polaron asymmetry (δ) and polaron weight (ρ). The ground state of the the QRM is non-degenerate so that the QFI takes the simplified form (20). Then, with the four variation resources, the QFI can be decomposed into different parts:

$$F_Q = F_Q^{x,x} + F_Q^{\xi,\xi} + F_Q^{\delta,\delta} + F_Q^{\rho,\rho} + F_Q^{x,\xi} + F_Q^{x,\rho} + F_Q^{x,\delta} + F_Q^{\rho,\xi} + F_Q^{\rho,\delta} + F_Q^{\xi,\delta} \quad (22)$$

where the first four terms are purely intra-resource contributions, while the others terms come from inter-resource interplays. We leave the definitions of these term in Appendix A.

We illustrate the different contributions of QFI in Fig.10. We see in Fig.10(a) that the pure displacement

part $F_Q^{x,x}$ (blue solid line) contribute a main portion in the total QFI F_Q^{Total} (dotted red line), while the intra-resource parts ($F_Q^{\xi,\xi}$, $F_Q^{\delta,\delta}$, $F_Q^{\rho,\rho}$) make relatively smaller contributions as shown in Fig. 10(b). Still, despite that the inter-resource terms $F_Q^{\rho,\xi}$, $F_Q^{\rho,\delta}$, $F_Q^{\xi,\delta}$ are small as in Fig. 10(d), we find in Fig. 10(c) that the polaron asymmetry (black dotted line) gives a considerable contribution via the interplay with the displacement.

C. Improvements on QFI and critical couplings

We finally present the results in symmetric and asymmetric polaron pictures in comparing the QFI and critical couplings with the numerically accurate results in ED. Indeed, as illustrated in Fig.10(a), both the symmetric [$\delta_i = 0$, green (light gray) solid line] and asymmetric [$\delta_i \neq 0$, green (dark gray) solid line] polaron pictures can capture the variations of the QFI extracted in ED (orange dotted line). At finite frequencies both the symmetric and asymmetric polaron pictures yield fairly accurate results illustrated by the frequency example $\omega/\Omega = 0.3$ in Fig. 10(b). However, discrepancy from the ED results arises in lower frequencies as $\omega/\Omega = 0.1$ in Fig. 10(c) in the close-up plot. Still, here we see that the asymmetric polaron picture leads to smaller discrepancy than the symmetric polaron picture, with both the peak values and positions of the QFI closer to that of ED as marked by the dots.

Figure 10(d) gives the frequency dependence of the critical couplings extracted from the peak position of the QFI. Indeed, the critical couplings at finite frequencies are not any more located at the low-frequency one g_{c0} as illustrated in Fig. 10(a), while g_c in Eq. (11), taken as the unit in the Fig. 10(d), captures better the right scale. Still, the accurate one is given by g_c^F (dashed line) in Eqs. (13) and (14). We see in the entire frequency regime that asymmetric polaron picture (blue solid line) considerably reduces the errors of the QFI peak values in Fig. 10(e) and critical-like couplings in Fig. 10(f). There is still some remnant errors, especially for the QFI peak values in low frequency limit, as we have only considered the lowest order of polaron asymmetry as in Eq. (9). The errors can be further reduced by including higher order approximations. Nevertheless, these results are enough to demonstrate that the effect of polaron asymmetry is innegligible and richer physics emerges in the presence of the polaron asymmetry.

VII. CONCLUSIONS

We have proposed the variational method in asymmetric polaron picture for the QRM. The method is capable of capturing the physics of polaron asymmetry arising from the tunneling energy and the potential gradient in the subtle energy competitions, which is missing in the

previous symmetric polaron picture. We have applied the method to study the ground state and first excited state. The results show that the asymmetric polaron picture not only yields accuracy improvements for the physical quantities but also enables us to extract several underlying transitions unnoticed in the symmetric polaron picture.

For the ground state we have found that the asymmetry effect for the polarons and antipolarons are quite considerable. We have seen the opposite asymmetry signs for the polarons and antipolarons, which indicates they are effectively attracting each other. Two transitions of asymmetry imbalance reversal appear at low frequencies, which reflects the delicate competition between the tunneling-induced asymmetry and the potential-gradient-induced potential asymmetry. We also notice that the polaron displacement is not only decided by the direct displacement renormalization but also much affected by the polaron asymmetry. We figure out a boundary of unnormal displacement renormalization beyond 1 existing for all frequencies, which is a sign of strong polaron asymmetry.

Despite that variational methods usually apply for the ground state, we have also utilized the asymmetric polaron picture to analyze the first excited state with good outcomes. Besides the maintained accuracy, we have unveiled some distinguished features and additional transitions different from the ground state. Indeed, the weights of the polarons and antipolarons have opposite signs and the magnitudes are both increasing in coupling reduction, in contrast to the same signs and decreasing polaron weight magnitude in the ground state. Apart from the main transition around g_c the same as the ground state, we have also found a transition of sign reversal for the polaron asymmetry factor, which indicates an attraction/repulsion shift for the polarons. Moreover, the positive parity also leads to a density cancellation between polarons and antipolarons, which results in a more explicit repulsion effect with a diverging displacement renormalization at small couplings for the final polaron peak.

We have finally applied the asymmetric polaron picture in quantum Fisher information analysis and critical coupling extraction, with improvements over the symmetric polaron picture in both these two properties. The improvements indicate that the polaron asymmetry makes a considerable contribution to the quantum resource in quantum metrology and plays an unneigligible role in the QPT.

Although the components of the QRM are finite and the model has been much studied [1–4, 7, 8, 23, 25–29, 34–41, 45, 46, 50, 55, 57–60, 69–105, 107–113, 116, 145, 146], our more-extracted results hint that the physics we could learn from the model might be infinite. The polaron picture is a useful method to analyze the QPTs in light-matter models [4, 26, 30, 31, 33, 35–39, 44, 70, 71], with high accuracy and transparent physical picture. The asymmetric polaron picture we develop

in this paper might help to deepen the physics exploration in road of reaching the ideal goal of full understanding.

As a final remark, although the present work is focusing on the QRM, our analysis can be extended to other light-matter models. Indeed, in more general models with the anisotropic coupling [14, 34, 37, 38, 82, 147–149] and the Stark coupling [33, 39, 41, 107–109, 111, 112, 146], the ground state before first topological transition is similar to that of the QRM considered here, while the second phase after the first topological transition is similar to the first excited state of the QRM [37–41]. Also, extensions to multiple-polaron case [38, 70] and the frequency dimension in nonlinear QRM [30–33, 71] are possible. These examples indicate that our asymmetric polaron picture could have broader applications, which may need more future works.

ACKNOWLEDGMENT

This work was supported by the National Natural Science Foundation of China (Grants No. 12474358 and No. 12247101).

Appendix A: Decomposed QFI in asymmetric polaron picture

As addressed in Sec. VIA, the QFI provides the upper bound of measurement precision in quantum metrology. Here in this Appendix we formulate the QFI in the asymmetric polaron picture developed in the main text. The wave function can be decomposed into a linear combination of n_p number of polarons

$$\psi_{\pm}(x) = \sum_{a=1}^{n_p} c_a^{\pm} \varphi_a^{\pm}(x) \quad (\text{A1})$$

where

$$\varphi_a^{\sigma}(x) = (1 + \delta_a^{\sigma} x_a^{\sigma}) \left(\frac{\xi_a^{\sigma}}{\pi} \right)^{1/4} \exp[-\frac{1}{2} \xi_a^{\sigma} (x + x_a^{\sigma})^2] \quad (\text{A2})$$

represents an asymmetric polaron labelled by a in the spin component $\sigma = \pm$. Generally one can adopt different polaron numbers, $n_p \geq 1$, depending on the approximation one takes. As a simplest description without loss of accuracy, in the present work we take $n_p = 2$ so that a sums over the polaron α and antipolaron β in the main text.

The variation of the wave function consists of the change resources of the displacement x_a^{\pm} , frequency renormalization ξ_a^{\pm} , polaron weight c_a^{\pm} and polaron asym-

metry δ_a^\pm in response to the variation of the coupling g

$$\begin{aligned} \frac{d\psi_\pm}{dg} &= \sum_a^{n_p} \left(c_a^\pm \frac{d\varphi_a^\pm}{dx_a^\pm} \frac{dx_a^\pm}{dg} + c_a^\pm \frac{d\varphi_a^\pm}{d\xi_a^\pm} \frac{d\xi_a^\pm}{dg} \right. \\ &\quad \left. + \frac{dc_a^\pm}{dg} \varphi_a^\pm + c_a^\pm \frac{d\varphi_a^\pm}{d\delta_a^\pm} \frac{d\delta_a^\pm}{dg} \right). \end{aligned} \quad (\text{A3})$$

Then, the QFI can be disassembled into intra-resource parts and inner-resource parts

$$\begin{aligned} F_Q &= F_Q^{x,x} + F_Q^{\xi,\xi} + F_Q^{\delta,\delta} + F_Q^{\rho,\rho} \\ &\quad + F_Q^{x,\xi} + F_Q^{x,\rho} + F_Q^{x,\delta} + F_Q^{\rho,\xi} + F_Q^{\rho,\delta} + F_Q^{\xi,\delta} \end{aligned} \quad (\text{A4})$$

The intra-resource parts can be formulated as

$$F_Q^{x,x} = \sum_a^{n_p} \sum_{a'}^{n_p} \sum_{\sigma=\pm} c_a^\sigma c_{a'}^\sigma \langle \frac{d\varphi_a^\sigma}{dx_a^\sigma} | \frac{d\varphi_{a'}^\sigma}{dx_{a'}^\sigma} \rangle \frac{dx_a^\sigma}{dg} \frac{dx_{a'}^\sigma}{dg}, \quad (\text{A5})$$

$$F_Q^{\xi,\xi} = \sum_a^{n_p} \sum_{a'}^{n_p} \sum_{\sigma=\pm} c_a^\sigma c_{a'}^\sigma \langle \frac{d\varphi_a^\sigma}{d\xi_a^\sigma} | \frac{d\varphi_{a'}^\sigma}{d\xi_{a'}^\sigma} \rangle \frac{d\xi_a^\sigma}{dg} \frac{d\xi_{a'}^\sigma}{dg}, \quad (\text{A6})$$

$$F_Q^{\delta,\delta} = \sum_a^{n_p} \sum_{a'}^{n_p} \sum_{\sigma=\pm} c_a^\sigma c_{a'}^\sigma \langle \frac{d\varphi_a^\sigma}{d\delta_a^\sigma} | \frac{d\varphi_{a'}^\sigma}{d\delta_{a'}^\sigma} \rangle \frac{d\delta_a^\sigma}{dg} \frac{d\delta_{a'}^\sigma}{dg}, \quad (\text{A7})$$

$$F_Q^{\rho,\rho} = \sum_a^{n_p} \sum_{a'}^{n_p} \sum_{\sigma=\pm} \langle \varphi_a^\sigma | \varphi_{a'}^\sigma \rangle \frac{dc_a^\sigma}{dg} \frac{dc_{a'}^\sigma}{dg}, \quad (\text{A8})$$

while inter-resource parts read

$$\begin{aligned} F_Q^{x,\xi} &= \sum_a^{n_p} \sum_{a' \neq a}^{n_p} \sum_{\sigma=\pm} \left(c_a^\sigma c_{a'}^\sigma \langle \frac{d\varphi_a^\sigma}{dx_a^\sigma} | \frac{d\varphi_{a'}^\sigma}{d\xi_{a'}^\sigma} \rangle \frac{dx_a^\sigma}{dg} \frac{d\xi_{a'}^\sigma}{dg} \right. \\ &\quad \left. + c_a^\sigma c_{a'}^\sigma \langle \frac{d\varphi_a^\sigma}{d\xi_a^\sigma} | \frac{d\varphi_{a'}^\sigma}{dx_{a'}^\sigma} \rangle \frac{d\xi_a^\sigma}{dg} \frac{dx_{a'}^\sigma}{dg} \right), \end{aligned} \quad (\text{A9})$$

$$\begin{aligned} F_Q^{x,\delta} &= \sum_a^{n_p} \sum_{a' \neq a}^{n_p} \sum_{\sigma=\pm} \left(c_a^\sigma c_{a'}^\sigma \langle \frac{d\varphi_a^\sigma}{dx_a^\sigma} | \frac{d\varphi_{a'}^\sigma}{d\delta_{a'}^\sigma} \rangle \frac{dx_a^\sigma}{dg} \frac{d\delta_{a'}^\sigma}{dg} \right. \\ &\quad \left. + c_a^\sigma c_{a'}^\sigma \langle \frac{d\varphi_a^\sigma}{d\delta_a^\sigma} | \frac{d\varphi_{a'}^\sigma}{dx_{a'}^\sigma} \rangle \frac{d\delta_a^\sigma}{dg} \frac{dx_{a'}^\sigma}{dg} \right), \end{aligned} \quad (\text{A10})$$

$$\begin{aligned} F_Q^{\xi,\delta} &= \sum_a^{n_p} \sum_{a' \neq a}^{n_p} \sum_{\sigma=\pm} \left(c_a^\sigma c_{a'}^\sigma \langle \frac{d\varphi_a^\sigma}{d\xi_a^\sigma} | \frac{d\varphi_{a'}^\sigma}{d\delta_{a'}^\sigma} \rangle \frac{d\xi_a^\sigma}{dg} \frac{d\delta_{a'}^\sigma}{dg} \right. \\ &\quad \left. + c_a^\sigma c_{a'}^\sigma \langle \frac{d\varphi_a^\sigma}{d\delta_a^\sigma} | \frac{d\varphi_{a'}^\sigma}{d\xi_{a'}^\sigma} \rangle \frac{d\delta_a^\sigma}{dg} \frac{d\xi_{a'}^\sigma}{dg} \right), \end{aligned} \quad (\text{A11})$$

$$\begin{aligned} F_Q^{\xi,\rho} &= \sum_a^{n_p} \sum_{a' \neq a}^{n_p} \sum_{\sigma=\pm} \left(c_a^\sigma \frac{d\xi_a^\sigma}{dg} \langle \frac{d\varphi_a^\sigma}{d\xi_a^\sigma} | \varphi_{a'}^\sigma \rangle \frac{dc_{a'}^\sigma}{dg} \right. \\ &\quad \left. + \frac{dc_a^\sigma}{dg} \langle \varphi_a^\sigma | \frac{d\varphi_{a'}^\sigma}{d\xi_{a'}^\sigma} \rangle c_{a'}^\sigma \frac{d\xi_{a'}^\sigma}{dg} \right), \end{aligned} \quad (\text{A12})$$

$$\begin{aligned} F_Q^{x,\rho} &= \sum_a^{n_p} \sum_{a' \neq a}^{n_p} \sum_{\sigma=\pm} \left(c_a^\sigma \frac{dx_a^\sigma}{dg} \langle \frac{d\varphi_a^\sigma}{dx_a^\sigma} | \varphi_{a'}^\sigma \rangle \frac{dc_{a'}^\sigma}{dg} \right. \\ &\quad \left. + \frac{dc_a^\sigma}{dg} \langle \varphi_a^\sigma | \frac{d\varphi_{a'}^\sigma}{dx_{a'}^\sigma} \rangle c_{a'}^\sigma \frac{dx_{a'}^\sigma}{dg} \right); \end{aligned} \quad (\text{A13})$$

$$\begin{aligned} F_Q^{\delta,\rho} &= \sum_a^{n_p} \sum_{a' \neq a}^{n_p} \sum_{\sigma=\pm} \left(c_a^\sigma \frac{dx_a^\sigma}{dg} \langle \frac{d\varphi_a^\sigma}{dx_a^\sigma} | \varphi_{a'}^\sigma \rangle \frac{dc_{a'}^\sigma}{dg} \right. \\ &\quad \left. + \frac{dc_a^\sigma}{dg} \langle \varphi_a^\sigma | \frac{d\varphi_{a'}^\sigma}{dx_{a'}^\sigma} \rangle c_{a'}^\sigma \frac{dx_{a'}^\sigma}{dg} \right). \end{aligned} \quad (\text{A14})$$

Here the overlaps of two wave packets φ_1, φ_2 are defined as the expectation integral

$$\langle \varphi_1 | \varphi_2 \rangle = \int_{-\infty}^{\infty} \varphi_1^*(x) \varphi_2(x) dx \quad (\text{A15})$$

while the derivative ones are similarly defined by replacing φ_i with the derivative $d\varphi_i/dp_i$ with respect to the parameter p_i . The analytic and explicit expressions of the derivative wave-packet overlaps are too lengthy to list here, nevertheless they can be readily obtained with Eq. (A2).

Appendix B: Variational expressions in asymmetric polaron picture

As introduced in Sec. III B in the main text, the variational energy is given by

$$E = \langle \Psi | H | \Psi \rangle = h_{++}^+ + \frac{1}{2} P \Omega n_{+-} + \varepsilon_0. \quad (\text{B1})$$

The general wave function Ψ is defined at Eq. (3), while the form in the asymmetric polaron picture is presented

in Eqs.(5)-(9). Under such a formalism, the first term in Eq. (B1)

$$\begin{aligned} h_{++}^+ &= \langle \psi | h^+ | \psi \rangle \\ &= \alpha^2 \langle \varphi_\alpha | h^+ | \varphi_\alpha \rangle + \beta^2 \langle \varphi_\beta | h^+ | \varphi_\beta \rangle \\ &\quad + 2\alpha\beta \langle \varphi_\alpha | h^+ | \varphi_\beta \rangle, \end{aligned} \quad (\text{B2})$$

gives the effective single-particle energy for $h^+ = \frac{1}{2}\omega[\hat{p}^2 + (\hat{x} + g')^2]$ with a constant energy $\varepsilon_0 = -\frac{1}{2}\omega(g'^2 + 1)$. The middle term in Eq. (B1) denotes the tunneling or spin-flipping energy with

$$\begin{aligned} n_{+-} &= \langle \psi | \bar{\psi} \rangle \\ &= \alpha^2 \langle \varphi_\alpha | \bar{\varphi}_\alpha \rangle + \beta^2 \langle \varphi_\beta | \bar{\varphi}_\beta \rangle \\ &\quad + 2\alpha\beta \langle \varphi_\alpha | \bar{\varphi}_\beta \rangle. \end{aligned} \quad (\text{B3})$$

The expectation factors can be obtained explicitly for intra-polaron term

$$\begin{aligned} &\langle \varphi_\alpha | h^+ | \varphi_\alpha \rangle \\ &= \frac{\omega}{8\xi_\alpha^2} \left[\delta_\alpha^2 \left(2(\zeta_\alpha - 1)^2 \xi_\alpha g'^2 + 3\xi_\alpha^2 + 3 \right) \right] \\ &+ \frac{\omega}{8\xi_\alpha^2} \left[2\xi_\alpha \left(2(\zeta_\alpha - 1)^2 \xi_\alpha g'^2 + \xi_\alpha^2 + 1 \right) \right] \\ &- \frac{\omega}{8\xi_\alpha^2} [8\delta_\alpha(\zeta_\alpha - 1)\xi_\alpha g'], \end{aligned} \quad (\text{B4})$$

inter-antipolaron term

$$\begin{aligned} &\langle \varphi_\alpha | h^+ | \varphi_\beta \rangle \\ &= f_1 \left\{ \xi_\alpha \xi_\beta \left[\xi_\beta^2 - \delta_\beta (\zeta_\beta + 1)^2 \xi_\beta (g')^3 (\zeta_\alpha + \zeta_\beta) + \delta_\beta g' (-3\zeta_\alpha + \zeta_\beta + 4) - (\zeta_\beta + 1) \xi_\beta (g')^2 (2\zeta_\alpha - \zeta_\beta - 3) + 2 \right] \right. \\ &\quad \left. + \xi_\beta^2 \left[2\delta_\beta (\zeta_\beta + 1) g' + (\zeta_\beta + 1)^2 \xi_\beta (g')^2 + 1 \right] \right\} \\ &+ f_1 \xi_\alpha^3 \left\{ \xi_\beta + \delta_\beta (g')^3 (\zeta_\alpha + \zeta_\beta) \left[\zeta_\alpha^2 (\xi_\beta^2 - 1) + 2\zeta_\alpha (\zeta_\beta \xi_\beta^2 + 1) + \zeta_\beta^2 \xi_\beta^2 - 1 \right] \right. \\ &\quad \left. - 3\delta_\beta \xi_\beta g' (\zeta_\alpha + \zeta_\beta) - (g')^2 \left[\zeta_\alpha^2 (\xi_\beta^2 - 1) + 2\zeta_\alpha (\zeta_\beta \xi_\beta^2 + 1) + \zeta_\beta^2 \xi_\beta^2 - 1 \right] \right\} \\ &+ f_1 \xi_\alpha^2 \left\{ 2\xi_\beta^2 + 2(\zeta_\alpha - 1) \delta_\beta (\zeta_\beta + 1) \xi_\beta (g')^3 (\zeta_\alpha + \zeta_\beta) - \delta_\beta g' \left[3\zeta_\alpha (\xi_\beta^2 + 1) + 3\zeta_\beta \xi_\beta^2 + \zeta_\beta - 2 \right] \right. \\ &\quad \left. - \xi_\beta (g')^2 \left[\zeta_\alpha^2 (\xi_\beta^2 - 1) + 2\zeta_\alpha (\zeta_\beta \xi_\beta^2 + \zeta_\beta + 2) + \zeta_\beta^2 \xi_\beta^2 - 2\zeta_\beta - 3 \right] + 1 \right\} \\ &+ f_2 \delta_\beta \left\{ \xi_\beta^2 \left[(\zeta_\beta + 1) \xi_\beta (g')^2 (2\zeta_\alpha + 3\zeta_\beta + 1) + 3 \right] \right. \\ &\quad \left. - \xi_\alpha \xi_\beta \left[-3(\xi_\beta^2 + 2) + (\zeta_\beta + 1)^2 \xi_\beta^2 (g')^4 (\zeta_\alpha + \zeta_\beta)^2 + 3(\zeta_\alpha - 1) \xi_\beta (g')^2 (\zeta_\alpha + 2\zeta_\beta + 1) \right] \right\} \\ &+ f_2 \delta_\beta \xi_\alpha^2 \left\{ 6\xi_\beta^2 + 2(\zeta_\alpha - 1) (\zeta_\beta + 1) \xi_\beta^2 (g')^4 (\zeta_\alpha + \zeta_\beta)^2 \right. \\ &\quad \left. - 3\xi_\beta (g')^2 \left[2\zeta_\alpha^2 \xi_\beta^2 + 2\zeta_\alpha (2\zeta_\beta \xi_\beta^2 + \zeta_\beta + 1) + \zeta_\beta^2 (2\xi_\beta^2 + 1) - 1 \right] + 3 \right\} \\ &+ f_2 \delta_\beta \xi_\alpha^3 \left\{ 3\xi_\beta + \xi_\beta (g')^4 (\zeta_\alpha + \zeta_\beta)^2 \left[\zeta_\alpha^2 (\xi_\beta^2 - 1) + 2\zeta_\alpha (\zeta_\beta \xi_\beta^2 + 1) + \zeta_\beta^2 \xi_\beta^2 - 1 \right] \right. \\ &\quad \left. - (g')^2 \left[\zeta_\alpha^2 (6\xi_\beta^2 - 3) + 2\zeta_\alpha \zeta_\beta (6\xi_\beta^2 - 1) + 4\zeta_\alpha + 6\xi_\beta^2 \xi_\beta^2 + 2\zeta_\beta - 1 \right] \right\}, \end{aligned} \quad (\text{B6})$$

and inter-spin terms

$$\langle \varphi_\alpha | \bar{\varphi}_\alpha \rangle = \frac{e^{-\zeta_\alpha^2 \xi_\alpha (g')^2}}{2\xi_\alpha} [2\xi_\alpha (\delta_\alpha \zeta_\alpha g' + 1)^2 - \delta_\alpha^2] \quad (\text{B7})$$

intra-antipolaron term

$$\begin{aligned} &\langle \varphi_\beta | h^+ | \varphi_\beta \rangle \\ &= \frac{\omega}{8\xi_\beta^2} \left[\delta_\beta^2 \left(2(\zeta_\beta + 1)^2 \xi_\beta g'^2 + 3\xi_\beta^2 + 3 \right) \right] \\ &+ \frac{\omega}{8\xi_\beta^2} \left[2\xi_\beta \left(2(\zeta_\beta + 1)^2 \xi_\beta g'^2 + \xi_\beta^2 + 1 \right) \right] \\ &+ \frac{\omega}{8\xi_\beta^2} [8\delta_\beta(\zeta_\beta + 1)\xi_\beta g'], \end{aligned} \quad (\text{B5})$$

where the coefficients are give by

$$f_1 = \frac{\omega \sqrt[4]{\xi_\alpha} \sqrt[4]{\xi_\beta}}{\sqrt{2}(\xi_\alpha + \xi_\beta)^{7/2}} \exp \left[\frac{\xi_\alpha \xi_\beta (g')^2 (\zeta_\alpha + \zeta_\beta)^2}{-2(\xi_\alpha + \xi_\beta)} \right] \quad (\text{B10})$$

-
- [1] D. Braak, *Phys. Rev. Lett.* **107**, 100401 (2011).
- [2] E. Solano, *Physics* **4**, 68 (2011).
- [3] A. Le Boité, *Adv. Quantum Technol.* **3**, 1900140 (2020).
- [4] J. Liu, M. Liu, Z.-J. Ying, and H.-G. Luo, *Adv. Quantum Technol.* **4**, 2000139 (2021).
- [5] C. Ciuti, G. Bastard, and I. Carusotto, *Phys. Rev. B* **72**, 115303 (2005).
- [6] A. A. Anappara, S. De Liberato, A. Tredicucci, C. Ciuti, G. Biasiol, L. Sorba, and F. Beltram, *Phys. Rev. B* **79**, 201303(R) (2009).
- [7] P. Forn-Díaz, L. Lamata, E. Rico, J. Kono, and E. Solano, *Rev. Mod. Phys.* **91**, 025005 (2019).
- [8] A. F. Kockum, A. Miranowicz, S. De Liberato, S. Savasta, and F. Nori, *Nat. Rev. Phys.* **1**, 19 (2019).
- [9] A. Wallraff, D. I. Schuster, A. Blais, L. Frunzio, R.-S. Huang, J. Majer, S. Kumar, S. M. Girvin, and R. J. Schoelkopf, *Nature* **431**, 162.
- [10] G. Günter, A. A. Anappara, J. Hees, A. Sell, G. Biasiol, L. Sorba, S. De Liberato, C. Ciuti, A. Tredicucci, A. Leitenstorfer, and R. Huber, *Nature* **458**, 178 (2009).
- [11] T. Niemczyk, F. Deppe, H. Huebl, E. P. Menzel, F. Hocke, M. J. Schwarz, J. J. Garcia-Ripoll, D. Zueco, T. Hümmer, E. Solano, A. Marx, and R. Gross, *Nat. Phys.* **6**, 772 (2010).
- [12] B. Peropadre, P. Forn-Díaz, E. Solano, and J. J. García-Ripoll, *Phys. Rev. Lett.* **105**, 023601 (2010).
- [13] P. Forn-Díaz, J. J. García-Ripoll, B. Peropadre, J.-L. Orgiazzi, M. A. Yurtalan, R. Belyansky, C. M. Wilson, and A. Lupascu, *Nat. Phys.* **13**, 39 (2017).
- [14] P. Forn-Díaz, J. Lisenfeld, D. Marcos, J. J. García-Ripoll, E. Solano, C. J. P. M. Harmans, and J. E. Mooij, *Phys. Rev. Lett.* **105**, 237001 (2010).
- [15] G. Scalari, C. Maisen, D. Turčinková, D. Hagenmüller, S. De Liberato, C. Ciuti, C. Reichl, D. Schuh, W. Wegscheider, M. Beck, and J. Faist, *Science* **335**, 1323 (2012).
- [16] Z.-L. Xiang, S. Ashhab, J. Q. You, and F. Nori, *Rev. Mod. Phys.* **85**, 623 (2013).
- [17] F. Yoshihara, T. Fuse, S. Ashhab, K. Kakuyanagi, S. Saito, and K. Semba, *Nat. Phys.* **13**, 44 (2017).
- [18] X. Gu, A. F. Kockum, A. Miranowicz, Y.-X. Liu, and F. Nori, *Physics Reports* **718-719**, 1 (2017).
- [19] A. Bayer, M. Pozimski, S. Schambeck, D. Schuh, R. Huber, D. Bougeard, and C. Lange, *Nano letters* **17**, 6340 (2017).
- [20] A. Stokes and A. Nazir, *Nat. Commun.* **10**, 499 (2019).
- [21] W. Qin, A. F. Kockum, C. S. Muñoz, A. Miranowicz, and F. Nori, *Phys. Rep.* **1078**, 1 (2024).
- [22] I. I. Rabi, *Phys. Rev.* **51**, 652 (1937).
- [23] D. Braak, Q.-H. Chen, M. T. Batchelor, and E. Solano, *J. Phys. A: Math. Theor.* **49**, 300301 (2016).
- [24] H.-P. Eckle, *Models of Quantum Matter* (Oxford University, Oxford, 2019).
- [25] S. Ashhab, *Phys. Rev. A* **87**, 013826 (2013).
- [26] Z.-J. Ying, M. Liu, H.-G. Luo, H.-Q. Lin, and J. Q. You, *Phys. Rev. A* **92**, 053823 (2015).
- [27] M.-J. Hwang, R. Puebla, and M. B. Plenio, *Phys. Rev. Lett.* **115**, 180404 (2015).
- [28] M.-J. Hwang and M. B. Plenio, *Phys. Rev. Lett.* **117**, 123602 (2016).
- [29] E. K. Irish and J. Larson, *J. Phys. A: Math. Theor.* **50**, 174002 (2017).
- [30] Z.-J. Ying, *Adv. Quantum Technol.* **8**, 2400630 (2025); *Adv. Quantum Technol.* **8**, 2570015 (2025), [Back Cover: (Adv. Quantum Technol. 7/2025)].
- [31] Z.-J. Ying, *Phys. Rev. A* **112**, 032626 (2025).
- [32] Z.-J. Ying, H.-H. Han, B.-J. Li, S. Felicetti, and D. Braak, *Adv. Quantum Technol.* **8**, e00263 (2025); *Adv. Quantum Technol.* **8**, e70061 (2025), [Back Cover: (Adv. Quantum Technol. 11/2025)].
- [33] Z.-J. Ying, *Phys. Rev. A* **112**, 052617 (2025).
- [34] M. Liu, S. Chesi, Z.-J. Ying, X. Chen, H.-G. Luo, and H.-Q. Lin, *Phys. Rev. Lett.* **119**, 220601 (2017).
- [35] Z.-J. Ying, L. Cong, and X.-M. Sun, *J. Phys. A: Math. Theor.* **53**, 345301 (2020), arXiv:1804.08128.
- [36] Z.-J. Ying, *Phys. Rev. A* **103**, 063701 (2021).
- [37] Z.-J. Ying, *Adv. Quantum Technol.* **5**, 2100088 (2022); *Adv. Quantum Technol.* **5**, 2270013 (2022), [Back Cover (Adv. Quantum Technol. 1/2022)].
- [38] Z.-J. Ying, *Adv. Quantum Technol.* **5**, 2100165 (2022).
- [39] Z.-J. Ying, *Adv. Quantum Technol.* **6**, 2200068 (2023); *Adv. Quantum Technol.* **6**, 2370011 (2023), [Front Cover (Adv. Quantum Technol. 1/2023)].
- [40] Z.-J. Ying, *Adv. Quantum Technol.* **6**, 2200177 (2023); *Adv. Quantum Technol.* **6**, 2370071 (2023), [Front Cover: (Adv. Quantum Technol. 7/2023)].
- [41] Z.-J. Ying, *Phys. Rev. A* **109**, 053705 (2024).
- [42] Z.-J. Ying, *Adv. Quantum Technol.* **7**, 2400053 (2024); *Adv. Quantum Technol.* **7**, 2470017 (2024), [Front Cover: (Adv. Quantum Technol. 7/2024)].
- [43] Z.-J. Ying, *Adv. Quantum Technol.* **7**, 2400288 (2024); *Adv. Quantum Technol.* **7**, 2470029 (2024), [Back Cover: (Adv. Quantum Technol. 10/2024)].
- [44] Z.-J. Ying, W.-L. Wang, and B.-J. Li, *Phys. Rev. A* **110**, 033715 (2024).
- [45] R. Grimaudo, A. S. Magalhães de Castro, A. Messina, E. Solano, and D. Valenti, *Phys. Rev. Lett.* **130**, 043602 (2023).
- [46] R. Grimaudo, D. Valenti, A. Sergi, and A. Messina, *Entropy* **25**, 187 (2023).
- [47] R. Grimaudo, G. Falci, A. Messina, E. Paladino, A. Sergi, E. Solano, and D. Valenti, *Phys. Rev. Res.* **6**, 043298 (2024).
- [48] G.-L. Zhu, C.-S. Hu, H. Wang, W. Qin, X.-Y. Lü, and F. Nori, *Phys. Rev. Lett.* **132**, 193602 (2024).
- [49] C. Liu and J.-F. Huang, *Sci. China Phys. Mech. Astron.* **67**, 210311 (2024).
- [50] J. Peng, E. Rico, J. Zhong, E. Solano, and I. L. Egusquiza, *Phys. Rev. A* **100**, 063820 (2019).
- [51] D. F. Padilla, H. Pu, G.-J. Cheng, and Y.-Y. Zhang, *Phys. Rev. Lett.* **129**, 183602 (2022).
- [52] S. Cheng, H.-G. Xu, X. Liu, and G. Xianlong, *Physica A* **604**, 127940 (2022).
- [53] S. Cheng, S.-P. Wang, G. D. M. Neto, and G. Xianlong, *Phys. Rev. A* **111**, 053501 (2025).
- [54] Q.-Y. Chen, F. Qiao, and Z.-J. Ying, arXiv:2511.14946 (2025), 10.48550/arxiv.2511.14946.
- [55] L. Garbe, M. Bina, A. Keller, M. G. A. Paris, and S. Felicetti, *Phys. Rev. Lett.* **124**, 120504 (2020).
- [56] V. Montenegro, U. Mishra, and A. Bayat, *Phys. Rev. Lett.* **126**, 200501 (2021).
- [57] Y. Chu, S. Zhang, B. Yu, and J. Cai, *Phys. Rev. Lett.*

- 126**, 010502 (2021).
- [58] L. Garbe, O. Abah, S. Felicetti, and R. Puebla, *Phys. Rev. Res.* **4**, 043061 (2022).
- [59] T. Ilias, D. Yang, S. F. Huelga, and M. B. Plenio, *PRX Quantum* **3**, 010354 (2022).
- [60] Z.-J. Ying, S. Felicetti, G. Liu, and D. Braak, *Entropy* **24**, 1015 (2022).
- [61] X. Zhu, J.-H. Lü, W. Ning, F. Wu, L.-T. Shen, Z.-B. Yang, and S.-B. Zheng, *Sci. China Phys. Mech. Astron.* **66**, 250313 (2023).
- [62] K. Gietka, C. Hotter, and H. Ritsch, *Phys. Rev. Lett.* **131**, 223604 (2023).
- [63] C. Hotter, H. Ritsch, and K. Gietka, *Phys. Rev. Lett.* **132**, 060801 (2024).
- [64] U. Alushi, W. Górecki, S. Felicetti, and R. Di Candia, *Phys. Rev. Lett.* **133**, 040801 (2024).
- [65] C. Mukhopadhyay and A. Bayat, *Phys. Rev. Lett.* **133**, 120601 (2024).
- [66] G. Mihailescu, A. Bayat, S. Campbell, and A. K. Mitchell, *Quantum Sci. Technol.* **9**, 035033 (2024).
- [67] C. Hotter, A. Miranowicz, and K. Gietka, *Phys. Rev. Lett.* **135**, 100802 (2025).
- [68] G. Mihailescu, U. Alushi, R. Di Candia, S. Felicetti, and K. Gietka, *arXiv:2510.02035* (2025).
- [69] S. Bera, S. Florens, H. U. Baranger, N. Roch, A. Nazir, and A. W. Chin, *Phys. Rev. B* **89**, 121108 (2014).
- [70] L. Cong, X.-M. Sun, M. Liu, Z.-J. Ying, and H.-G. Luo, *Phys. Rev. A* **95**, 063803 (2017).
- [71] L. Cong, X.-M. Sun, M. Liu, Z.-J. Ying, and H.-G. Luo, *Phys. Rev. A* **99**, 013815 (2019).
- [72] Q.-H. Chen, C. Wang, S. He, T. Liu, and K.-L. Wang, *Phys. Rev. A* **86**, 023822 (2012).
- [73] D. Braak, *Symmetry* **11**, 1259 (2019).
- [74] F. A. Wolf, M. Kollar, and D. Braak, *Phys. Rev. A* **85**, 053817 (2012).
- [75] S. Felicetti and A. Le Boit  , *Phys. Rev. Lett.* **124**, 040404 (2020).
- [76] S. Felicetti, D. Z. Rossatto, E. Rico, E. Solano, and P. Forn-D  az, *Phys. Rev. A* **97**, 013851 (2018).
- [77] S. Felicetti, J. S. Pedernales, I. L. Egusquiza, G. Romero, L. Lamata, D. Braak, and E. Solano, *Phys. Rev. A* **92**, 033817 (2015).
- [78] S. Felicetti, M.-J. Hwang, and A. Le Boit  , *Phys. Rev. A* **98**, 053859 (2018).
- [79] U. Alushi, T. Ramos, J. J. Garc  a-Ripoll, R. Di Candia, and S. Felicetti, *PRX Quantum* **4**, 030326 (2023).
- [80] E. K. Irish and J. Gea-Banacloche, *Phys. Rev. B* **89**, 085421 (2014).
- [81] E. K. T. Irish and A. D. Armour, *Phys. Rev. Lett.* **129**, 183603 (2022).
- [82] Q.-T. Xie, S. Cui, J.-P. Cao, L. Amico, and H. Fan, *Phys. Rev. X* **4**, 021046 (2014).
- [83] M. T. Batchelor and H.-Q. Zhou, *Phys. Rev. A* **91**, 053808 (2015).
- [84] Q. Xie, H. Zhong, M. T. Batchelor, and C. Lee, *J. Phys. A: Math. Theor.* **50**, 113001 (2017).
- [85] L. Garbe, I. L. Egusquiza, E. Solano, C. Ciuti, T. Coudreau, P. Milman, and S. Felicetti, *Phys. Rev. A* **95**, 053854 (2017).
- [86] L. Duan, Y.-F. Xie, D. Braak, and Q.-H. Chen, *J. Phys. A: Math. Theor.* **49**, 464002 (2016).
- [87] R. J. A. Rico, F. H. Maldonado-Villamizar, and B. M. Rodriguez-Lara, *Phys. Rev. A* **101**, 063825 (2020).
- [88] A. Le Boit  , M.-J. Hwang, H. Nha, and M. B. Plenio, *Phys. Rev. A* **94**, 033827 (2016).
- [89] A. Ridolfo, M. Leib, S. Savasta, and M. J. Hartmann, *Phys. Rev. Lett.* **109**, 193602 (2012).
- [90] Z.-M. Li, D. Ferri, D. Tilbrook, and M. T. Batchelor, *J. Phys. A: Math. Theor.* **54**, 405201 (2021).
- [91] K. K. W. Ma, *Phys. Rev. A* **102**, 053709 (2020).
- [92] Y.-Y. Zhang, *Phys. Rev. A* **94**, 063824 (2016).
- [93] Z. L  , C. Zhao, and H. Zheng, *J. Phys. A: Math. Theor.* **50**, 074002 (2017).
- [94] L.-T. Shen, Z.-B. Yang, H.-Z. Wu, and S.-B. Zheng, *Phys. Rev. A* **95**, 013819 (2017).
- [95] Y. Yan, Z. L  , L. Chen, and H. Zheng, *Advanced Quantum Technologies* **6**, 2200191 (2023).
- [96] X. Chen, Z. Wu, M. Jiang, X.-Y. L  , X. Peng, and J. Du, *Nat. Commun.* **12**, 6281 (2021).
- [97] M. Liu, Z.-J. Ying, J.-H. An, and H.-G. Luo, *New Journal of Physics* **17**, 043001 (2015).
- [98] Y. Zhang, G. Chen, L. Yu, Q. Liang, J.-Q. Liang, and S. Jia, *Phys. Rev. A* **83**, 065802 (2011).
- [99] L. Yu, S. Zhu, Q. Liang, G. Chen, and S. Jia, *Phys. Rev. A* **86**, 015803 (2012).
- [100] T. Liu, M. Feng, W. L. Yang, J. H. Zou, L. Li, Y. X. Fan, and K. L. Wang, *Phys. Rev. A* **88**, 013820 (2013).
- [101] V. V. Mangazeev, M. T. Batchelor, and V. V. Bazhanov, *J. Phys. A: Math. Theor.* **54**, 12LT01 (2021).
- [102] Z.-M. Li and M. T. Batchelor, *Phys. Rev. A* **103**, 023719 (2021).
- [103] C. Reyes-Bustos, D. Braak, and M. Wakayama, *J. Phys. A: Math. Theor.* **54**, 285202 (2021).
- [104] J. Casanova, R. Puebla, H. Moya-Cessa, and M. B. Plenio, *npj Quantum Information* **4**, 47 (2018).
- [105] J. Larson and T. Mavrogordatos, *The Jaynes-Cummings Model and Its Descendants* (IOP, London, 2021).
- [106] J.-F. Huang, J.-Q. Liao, and L.-M. Kuang, *Phys. Rev. A* **101**, 043835 (2020).
- [107] H.-P. Eckle and H. Johannesson, *J. Phys. A: Math. Theor.* **50**, 294004 (2017); *J. Phys. A: Math. Theor.* **56**, 345302 (2023).
- [108] A. L. Grimsmo and S. Parkins, *Phys. Rev. A* **87**, 033814 (2013).
- [109] A. L. Grimsmo and S. Parkins, *Phys. Rev. A* **89**, 033802 (2014).
- [110] X.-Y. L  , L.-L. Zheng, G.-L. Zhu, and Y. Wu, *Phys. Rev. Appl.* **9**, 064006 (2018).
- [111] Y.-F. Xie, L. Duan, and Q.-H. Chen, *J. Phys. A: Math. Theor.* **52**, 245304 (2019).
- [112] L. Cong, S. Felicetti, J. Casanova, L. Lamata, E. Solano, and I. Arrazola, *Phys. Rev. A* **101**, 032350 (2020).
- [113] Y.-Q. Shi, L. Cong, and H.-P. Eckle, *Phys. Rev. A* **105**, 062450 (2022).
- [114] W. Qin, A. Miranowicz, P.-B. Li, X.-Y. L  , J. Q. You, and F. Nori, *Phys. Rev. Lett.* **120**, 093601 (2018).
- [115] X.-F. Pan, P.-B. Li, X.-L. Hei, X. Zhang, M. Mochizuki, F.-L. Li, and F. Nori, *Phys. Rev. Lett.* **132**, 193601 (2024).
- [116] J. Peng, J. Zheng, J. Yu, P. Tang, G. A. Barrios, J. Zhong, E. Solano, F. Albarr  n-Arriagada, and L. Lamata, *Phys. Rev. Lett.* **127**, 043604 (2021).
- [117] H.-G. Xu, V. Montenegro, G. Xianlong, J. Jin, and G. D. d. M. Neto, *Phys. Rev. Res.* **6**, 013001 (2024).
- [118] S.-P. Wang, A. Ridolfo, T. Li, S. Savasta, F. Nori, Y. Nakamura, and J. Q. You, *Nat. Commun.* **14**, 4397 (2023).

- [119] E. T. Jaynes and F. W. Cummings, Proceedings of the IEEE **51**, 89 (1963).
- [120] E. K. Twyeffort Irish, Phys. Rev. Lett. **99**, 173601 (2007).
- [121] E. K. Twyeffort Irish, J. Gea-Banacloche, I. Martin, and K. C. Schwab, Phys. Rev. B **72**, 195410 (2005).
- [122] M.-J. Hwang and M.-S. Choi, Phys. Rev. A **82**, 025802 (2010).
- [123] G. Romero, D. Ballester, Y. M. Wang, V. Scarani, and E. Solano, Phys. Rev. Lett. **108**, 120501 (2012).
- [124] R. Stassi, M. Cirio, and F. Nori, npj Quantum Information **6**, 67 (2020).
- [125] R. Stassi and F. Nori, Phys. Rev. A **97**, 033823 (2018).
- [126] V. Macrì, F. Nori, and A. F. Kockum, Phys. Rev. A **98**, 062327 (2018).
- [127] F. Nagasawa, D. Frustaglia, H. Saarikoski, K. Richter, and J. Nitta, Nat. Commun. **4**, 2526 (2013).
- [128] Z.-J. Ying, P. Gentile, C. Ortix, and M. Cuoco, Phys. Rev. B **94**, 081406(R) (2016).
- [129] Z.-J. Ying, M. Cuoco, C. Ortix, and P. Gentile, Phys. Rev. B **96**, 100506(R) (2017).
- [130] Z.-J. Ying, P. Gentile, J. P. Baltanás, D. Frustaglia, C. Ortix, and M. Cuoco, Phys. Rev. Res. **2**, 023167 (2020).
- [131] P. Gentile, M. Cuoco, O. M. Volkov, Z.-J. Ying, I. J. VeraMarun, D. Makarov, and C. Ortix, Nature Electronics **5**, 551 (2022).
- [132] V. Galitski and I. B. Spielman, Nature **494**, 49 (2013).
- [133] Y.-J. Lin, K. Jiménez-García, and I. B. Spielman, Nature **471**, 83 (2011).
- [134] Y. Liu and Z.-J. Ying, Adv. Quantum Technol. **8**, e00431 (2025); Adv. Quantum Technol. **8**, e70062 (2025), [Front Cover: (Adv. Quantum Technol. 11/2025)].
- [135] Y. Liu and Z.-J. Ying, Adv. Quantum Technol. **8**, e00475 (2025).
- [136] J. E. Mooij, T. P. Orlando, L. Levitov, L. Tian, C. H. van der Wal, and S. Lloyd, Science **285**, 1036 (1999).
- [137] S. L. Braunstein and C. M. Caves, Phys. Rev. Lett. **72**, 3439 (1994).
- [138] M. M. Taddei, B. M. Escher, L. Davidovich, and R. L. de Matos Filho, Phys. Rev. Lett. **110**, 050402 (2013).
- [139] M. M. Rams, P. Sierant, O. Dutta, P. Horodecki, and J. Zakrzewski, Phys. Rev. X **8**, 021022 (2018).
- [140] S.-J. Gu, Int. J. Mod. Phys. B **24**, 4371 (2010).
- [141] W.-L. You, Y.-W. Li, and S.-J. Gu, Phys. Rev. E **76**, 022101 (2007).
- [142] W.-L. You and L. He, J. Phys.: Condens. Matter **27**, 205601 (2015).
- [143] H.-Q. Zhou and J. P. Barjaktarević, J. Phys. A: Math. Theor. **41**, 412001 (2008).
- [144] P. Zanardi and N. Paunković, Phys. Rev. E **74**, 031123 (2006).
- [145] B.-L. You, X.-Y. Liu, S.-J. Cheng, C. Wang, and X.-L. Gao, Acta Phys. Sin. **70**, 100201 (2021).
- [146] A. J. Maciejewski, M. Przybylska, and T. Stachowiak, Phys. Lett. A **378**, 3445 (2014).
- [147] I. Pietikäinen, S. Danilin, K. S. Kumar, A. Vepsäläinen, D. S. Golubev, J. Tuorila, and G. S. Paraoanu, Phys. Rev. B **96**, 020501 (2017).
- [148] Y. Wang, W.-L. You, M. Liu, Y.-L. Dong, H.-G. Luo, G. Romero, and J. Q. You, New Journal of Physics **20**, 053061 (2018).
- [149] G. Wang, R. Xiao, H. Z. Shen, and K. Xue, Sci. Rep. **9**, 4569 (2019).